THE ROYAL SOCIETY

The oscillatory channel flow with large wall injection

By Joseph Majdalani[1] and Tae-Seong Roh[2]

[1]*Department of Mechanical and Industrial Engineering,*
Marquette University, Milwaukee, WI 53233, USA
[2]*Department of Mechanical Engineering, California Institute of Technology,*
Pasadena, CA 91125, USA

In the presence of small-amplitude pressure oscillations, the linearized Navier–Stokes equations are solved to obtain an accurate description of the time-dependent field in a channel having a rectangular cross-section and two equally permeable walls. The mean solution is based on Taylor's classic profile, while the temporal solution is synthesized from irrotational and rotational fields. Using standard perturbation tools, the rotational component of the solution is derived from the linearized vorticity transport equation. In the absence of an exact solution to rely on, asymptotic formulations are compared with numerical simulations. In essence, the analytical formulation reveals rich vortical structures and discloses the main link between pressure oscillations and rotational wave formation. In the process, the explicit roles of variable injection, viscosity and oscillation frequency are examined. Using an alternative methodology, both WKB and multiple-scale techniques are applied to the linearized momentum equation. The momentum equation is of the boundary-value type and contains two small perturbation parameters. The primary and secondary parameters are, respectively, the reciprocals of the kinetic Reynolds and Strouhal numbers. The multiple-scale procedure employs two fictitious scales in space: a base and an undetermined scale. The latter is left unspecified during the derivation process until flow parameters are obtained in general form. Physical arguments are later used to define the arbitrary scale, which could not have been conjectured *a priori*. The emerging multiple-scale solution offers several advantages. Its leading-order term is simpler and more accurate than other formulations. Most of all, it clearly displays the relationship between the physical parameters that control the final motion. It thus provides the necessary means to quantify important flow features. These include the corresponding vortical wave amplitude, rotational depth of penetration, near-wall velocity overshoot and surfaces of constant phase. In particular, it discloses a viscous parameter that has a strong influence on the depth of penetration, and furnishes a closed-form expression for the maximum penetration depth in any oscillation mode. These findings enable us to quantify the location of the shear layer and corresponding penetration depth. By way of theoretical verification, comparisons between asymptotic formulations and numeric predictions are reassuring. The most striking result is, perhaps, the satisfactory agreement found between asymptotic predictions and data obtained, totally independently, from numerical simulations of the nonlinear Navier–Stokes equations. In closing, a standard error analysis is used to confirm

Proc. R. Soc. Lond. A (2000) **456**, 1625–1657

© 2000 The Royal Society

1625

that the absolute error associated with the analytic formulations exhibits the correct asymptotic behaviour.

1. Introduction

In this paper, we consider a weakly oscillatory flow inside a long and narrow channel with porous walls. In this problem, the mean fluid motion is induced by large injection at the walls. In addition to the mean motion, the presence of small-amplitude oscillatory waves must be accounted for. These waves are due to self-excited pressure disturbances that are caused by inevitable fluctuations in the injection rate. The strong coupling between oscillatory pressure gradients and mean fluid motion entails complex structures that we wish to describe. Such structures can arise in a number of engineering applications that involve unsteady flows inside enclosures with transpiring walls. For example, transpiring walls can be used to simulate surface ablation, phase sublimation and the burning of solid propellant slabs. Relevant applications may thus include rocket propulsion, filtration mechanisms, sweat cooling, chemical dispensing and other membrane separation processes. In order to develop asymptotic formulations for the problem at hand, the total solution will be synthesized from its mean and time-dependent components. The total solution will thus depend on an accurate definition of the steady field. The latter has been addressed previously by a number of investigators.

Characterization of steady fluid motions in porous channels may be traced back to the pioneering works of Berman (1953). In fact, assuming a similarity transformation, Berman investigated the laminar two-dimensional flow of an incompressible fluid driven by uniform injection inside a rectangular channel with porous walls. His motivation was the industrial separation of U_{235} from U_{238} by gaseous diffusion. He thus reduced the Navier–Stokes equations to a single nonlinear fourth-order differential equation with four boundary conditions and a cross-flow Reynolds number R. The latter was based on the normal injection speed v_w and channel half-spacing h. Being unable to solve the resulting equation in general form, Berman employed a regular perturbation scheme to produce an asymptotic formulation for small R. Numerous studies of channel flows with permeable walls followed.

For large suction, Sellars (1955) obtained the first term of an approximation that was further expanded by Terrill (1964). Using an integral approach, Proudman (1960) investigated the large R case with both equal and dissimilar injection or suction velocities. Using numerical curve-fitting principles, Morduchow (1957) invoked the method of averages to arrive at simple approximations over the entire injection range. For similar reasons, White *et al.* (1958), provided, for arbitrary R, an absolutely convergent power series whose coefficients were relegated to numerical routines. Other authors considered the large-suction case, including Robinson (1976), Lu *et al.* (1992), MacGillivray & Lu (1994) and Cox & King (1997).

For large injection, two contemporaneous and independently derived solutions were reported by Taylor (1956) and Yuan (1956). The former was a subset of the latter in the limiting case of an infinite R. The inability of Yuan's regular perturbation expansion to incorporate the viscous layer near the core was overcome by Terrill (1965), who employed matched asymptotic expansions to capture the inner layer.

The spatial stability of steady solutions of the Berman equation was also addressed by several authors. These included Varapaev & Yagodkin (1969), Raithby & Knudsen (1974), Hocking (1975), Sviridenkov & Yagodkin (1976), Brady (1984) and Durlofsky & Brady (1984). Some of their results suggested that injection flows tended to be absolutely stable and well behaved, asymptotically in R, and that increasing R reduced the steady flow development length. Conversely, suction flows appeared to be amenable to instability and reversal, exhibiting inflection points and dual solutions in some ranges of R.

The proof of solution multiplicity over different ranges of R has also attracted the attention of several mathematicians. Insofar as injection is concerned, Skalak & Wang (1978) were the first to report a unique solution for all R. Their formal conclusion was confirmed in a rigorous fashion by both Shih (1987) and Hastings *et al.* (1992).

Recently, the temporal stability of such flows has received attention *vis-à-vis* studies made by Zaturska *et al.* (1988), Taylor *et al.* (1991) and Watson *et al.* (1991). Such studies agreed that steady symmetric flows corresponding to the wall injection type were stable to time-dependent perturbations. Temporal stability has been considered also by Cox (1991).

While the majority of these pioneering studies relied on numerical simulations for validation purposes, some drew conclusions from experimental observations. In fact, laboratory experiments on steady channel flow through porous sheets were conducted by Taylor (1956), Varapaev & Yagodkin (1969), Raithby & Knudsen (1974) and Sviridenkov & Yagodkin (1976). These indicated that Taylor's or Yuan's similarity solutions with injection were observed to develop rapidly within the channel.

The addition of longitudinal pressure oscillations in channels with plane porous walls was realized experimentally by Ma *et al.* (1991), Barron *et al.* (1998), Avalon *et al.* (1998) and Casalis *et al.* (1998). Both Ma and Barron borrowed the concept of producing an alternating flow by external means from Richardson & Tyler (1929), who used electric motors to control the reciprocating motion of a piston mounted at the end of a crank. Naturally, the to-and-fro piston motion caused the injected gas inside the channel to vibrate harmonically. In both instances, carbon dioxide was expelled from flat blocks of sublimating dry ice to simulate the injectant. More recently, Avalon *et al.* (1998) and Casalis *et al.* (1998) demonstrated the existence of intrinsic self-induced harmonic oscillations in their experimental facility. Their apparatus comprised a long channel with two opposing permeable and impermeable walls. As uniform air injection was maintained through the plane porous sections of their apparatus, small unavoidable fluctuations in the injectant rate led to the onset of a strong acoustic environment. In all three experiments, the placement of a choked orifice or nozzle at the downstream end determined whether the oscillation mode character was of the closed–closed or closed–open type. In this paper, we shall focus on the basic laminar flow model that corresponds to pressure oscillations of the closed–closed type.

The objective will be, therefore, to derive an accurate asymptotic solution to the two-dimensional oscillatory field in a channel with plane porous walls. We hope that the detailed knowledge we gain will help develop physical intuition into more realistic flows in channels and tubes.

The forthcoming treatment is organized in the following manner. We start in § 2 by defining the geometry at hand, Berman's mean flow solution and fundamental
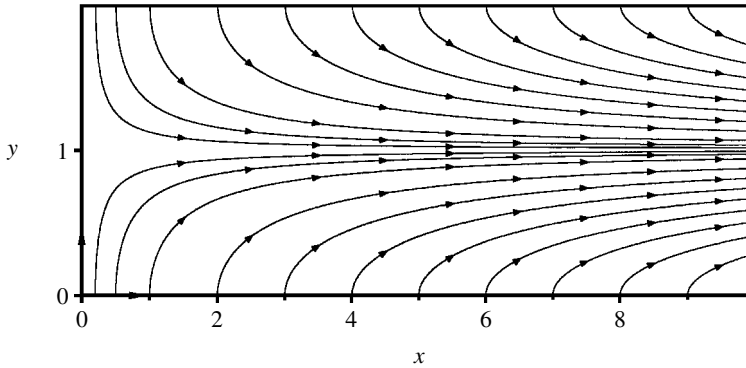
Figure 1. Two-dimensional mean flow streamlines.

criteria. This is followed in § 3 by linearizing the Navier–Stokes equations via regular perturbations in the injection Mach number and fluctuating pressure amplitude. In § 4 we employ a powerful theorem that permits decomposing the time-dependent field into irrotational and solenoidal components. While the irrotational pressure-driven solution can be obtained rather straightforwardly, the solenoidal vorticity-driven component demands a careful treatment and is deferred to § 5. Results are compared with numerical solutions of the linearized Navier–Stokes equations in § 6. In the ensuing discussion, the time-dependent vortical structure is closely examined. Since one would expect the transpiring walls to become inactive when injection is suppressed, our asymptotic formulation is compared with the corresponding exact solution of the Stokes type for a plane periodic flow between parallel walls.

To complete our flow field investigation, we extend our work by devising alternative formulations. These have the capability of elucidating the boundary layer structure and corresponding flow characteristics. To that end, we develop a more sophisticated strategy, based on WKB and multiple-scale theories, to obtain a more accurate and yet simpler representation of the velocity field. In the process, we introduce a space-reductive procedure that holds several advantages over our former perturbation solution set out in § 6. Thus, by devising alternative formulations, we are able to achieve two additional objectives: to confirm the validity of the former asymptotic solution, and to obtain closed-form expressions for the boundary-layer thickness and other important flow features. Instead of working with the vorticity transport equation, the velocity will now be derived directly from the momentum equation. This can be accomplished in § 7 via separation of variables but will result in a singular ordinary differential equation. We proceed thereafter by expanding the separated equation via WKB and two-variable multiple scales.

As we insist on verifications, results from the multiple-scale solution are compared with the former solution in § 8. This is accompanied by comparisons with computational data acquired from numerical simulations of the complete Navier–Stokes equations in their nonlinear form. Having established a high level of confidence in the asymptotic formulations, the Richardson velocity overshoot factor is evaluated in both magnitude and location. The penetration depth is also quantified. The error associated with the multiple-scale expansion is computed and compared with its precursor. Finally, we recapitulate and conclude the analysis in § 9.

2. Model description

(a) Geometry

The flow to be studied is established inside a long rectangular channel of length L, width w and bounded by plane porous walls that are $2h$ apart. Through these walls, a Newtonian fluid is injected with constant uniform velocity v_w. In this article, we shall, in fact, limit our attention to a perfect gas. Taking one side of the cross-section to be smaller than the other two sides enables us to treat the problem as a case of two-dimensional flow. We note parenthetically that it has been demonstrated by Terrill (1964, pp. 309–310) that the ratio of the width to the height of the channel does not have to be large to justify ignoring the influence of passive side walls. In addition, symmetry reduces the solution domain by half, making it sufficient to investigate the flow behaviour over half of the channel. This is especially true since, for large injection (see, for example, Zaturska *et al.* 1988), one expects unique, stable and symmetric temporal solutions about the channel's centreline. As shown schematically in figure 1, a coordinate system can be chosen with the origin at the porous wall. After normalizing all spatial coordinates by h, the streamwise, transverse and spanwise coordinates are denoted by x, y and z, respectively. The benefit of selecting y to be the normal distance measured from the wall will become apparent in later discussions of boundary-layer issues. Disregarding the influence of rigid boundaries, we assume no variations in z and confine our solution to $0 \leqslant x \leqslant l$, and $0 \leqslant y \leqslant 1$, where $l = L/h$.

When the channel is closed at the head end and choked at the downstream end, small fluctuations in the injectant rate give rise to harmonic pressure oscillations. These small pressure fluctuations can, in turn, couple with the mean flow to induce a time-dependent field that we wish to investigate. The streamlines depicted in figure 1 correspond to typical flow patterns pertaining to the undisturbed state.

(b) Criteria

In seeking a closed-form solution, several criteria must be met. In connection with the mean flow motion, we require that steady conditions prevail in a laminar, rotational and incompressible regime. Furthermore, neither swirling nor mixing can take place between incoming streams. The condition of uniform porosity is simulated by prescribing a constant normal velocity at the wall that is independent of position. On the one hand, we limit our scope to cross-flow Reynolds numbers satisfying $R = v_w h/\nu > 20$, where ν is the kinematic viscosity. The advantage is that, in this range, the mean flow can be adequately expressed by the well-known Taylor solution. The upper limit imposed on R is decreed, on the other hand, by the need to maintain an injection Mach number $M = v_w/a_s$ of order 10^{-3}, with a_s referring to the stagnation speed of sound. The reason is this: in linearizing the Navier–Stokes equations, M will be employed as a perturbation parameter. Consequently, the final formulation will entail an error of $\mathcal{O}(M)$. As a_s far exceeds v_w in most applications, M will be small in practice.

In what concerns the harmonic field performing small oscillations about the base flow, we constrain the oscillatory pressure amplitude A to remain small when compared with the stagnation pressure p_s evaluated at $x = 0$. This enables us to construct another small parameter that scales with A/p_s. Since the mean pressure decreases

in the streamwise direction, we limit the channel length to $l < 100$, for consistency in perturbation levels. Finally, we assume that the presence of isentropic oscillations does not affect the bulk fluid motion.

(c) Mean flow definition

In the absence of harmonic disturbances, the Navier–Stokes equations can be solved exactly using a similarity transformation. As demonstrated by Berman (1953), when the steady stream function Ψ is taken to vary linearly in the streamwise direction, namely $\Psi = -xF(y)$, one can write (following Varapaev & Yagodkin (1969) or Proudman (1960)), $(u_0, v_0) = (-xF', F)$, where $\boldsymbol{u}_0 = u_0\boldsymbol{i} + v_0\boldsymbol{j}$ is the mean velocity vector normalized by v_{w}. The separable component F must satisfy Berman's equation,

$$F'''' + R(F'F'' - FF''') = 0,$$

which depends on R and four boundary conditions: $F'(0) = F(1) = F''(1) = 0$ and $F(0) = 1$. Note that, in our notation, we follow Morduchow (1957) and Terrill (1965) in defining R to be positive for injection. With this choice, the unstable solution reported by Zaturska et al. (1988) will correspond to the $R < -6$ suction range. Although it is possible to manage a time-dependent formulation for arbitrary F, we are inclined to use a simple and practical solution corresponding to $F = \cos(\frac{1}{2}\pi y)$, which becomes exact as $R \to \infty$. More sophisticated Berman functions can give rise to technical issues that tend to complicate and slightly obscure the necessary analysis. This ideal solution, attributed to Taylor (1956), has been thoroughly verified both numerically and experimentally to be a reasonable approximation for $R > 20$. In this range, Varapaev & Yagodkin (1969) notes minimal solution changes and almost no changes for $R > 100$. With this choice of F, the velocity and vorticity fields can be expressed by

$$u_0 = \tfrac{1}{2}\pi x \sin(\tfrac{1}{2}\pi y), \quad v_0 = \cos(\tfrac{1}{2}\pi y) \quad \text{and} \quad \omega_0 = -\tfrac{1}{4}\pi^2 x \cos(\tfrac{1}{2}\pi y), \qquad (2.1)$$

which satisfy all the boundary conditions, including the no-slip at the wall. After normalizing the mean pressure by γp_{s} (where γ is the ratio of specific heats), one can integrate the ideal momentum equation to get

$$p_0(x,y) = 1/\gamma - \tfrac{1}{2}M^2[\tfrac{1}{4}\pi^2 x^2 + \cos^2(\tfrac{1}{2}\pi y)] = 1/\gamma + \mathcal{O}(M^2 x^2). \qquad (2.2)$$

The last formula makes it abundantly clear that the error associated with a uniform mean pressure assumption will be less than a few per cent when $x \leqslant 100$. Were it not for this limitation, our analysis would have been applicable to a semi-infinite channel.

3. Linearized Navier–Stokes equations

(a) Fundamental equations

Assuming constant kinematic viscosity and negligible bulk viscosity, the differential conservation of mass and momentum can be cast into the familiar non-dimensional form,

$$\frac{\partial \rho}{\partial t} + \nabla \cdot (\rho \boldsymbol{u}) = 0, \qquad (3.1)$$

$$\rho\left[\frac{\partial \boldsymbol{u}}{\partial t} + (\boldsymbol{u} \cdot \nabla)\boldsymbol{u}\right] = -\nabla p + \bar{R}^{-1}[\tfrac{4}{3}\nabla(\nabla \cdot \boldsymbol{u}) - \nabla \times (\nabla \times \boldsymbol{u})], \qquad (3.2)$$

where the total instantaneous velocity $\boldsymbol{u}$ is normalized by the speed of sound a_s, spatial coordinates by h, and time is made dimensionless by reference to h/a_s, the average time it takes for a pressure disturbance to travel from the wall to the core. Using asterisks for dimensional variables, the instantaneous pressure and density can be referenced to stagnation conditions. Setting $p \equiv p^*/(\gamma p_\mathrm{s})$, $\rho \equiv \rho^*/\rho_\mathrm{s}$, the acoustic Reynolds number $\bar{R}$ that appears in (3.2) will be $a_\mathrm{s} h/\nu$.

(b) Variable decomposition

When periodic oscillations are introduced at a radian frequency k, the instantaneous pressure can be written as a sum of its steady and fluctuating components. Using subscripts for perturbation orders, the total pressure can be expanded into

$$p^* = p_0^*(x^*, y^*) + p_1^*(x^*, y^*, t^*) = p_0^* + AP(x^*, y^*) \exp(-ikt^*), \qquad (3.3)$$

where P is a function of $\mathcal{O}(1)$ that will be determined in § 4 d. Normalizing and using $p_0^* = p_\mathrm{s}$, we get

$$p(x, y, t) = 1/\gamma + \bar{\varepsilon} P(x, y) \exp(-ik_m t) + \mathcal{O}(M^2 x^2) \cong 1/\gamma + \bar{\varepsilon} p_1(x, y, t), \qquad (3.4)$$

where $k_m = kh/a_\mathrm{s}$ is the non-dimensional frequency, and $\bar{\varepsilon} = A/(\gamma p_\mathrm{s})$ is the pressure wave amplitude. Other fluctuating variables can be expanded in a similar fashion. For example, one can define $\rho_1^* \equiv \bar{\varepsilon} \rho_\mathrm{s} \rho_1$ and $\boldsymbol{u}_1^* \equiv \bar{\varepsilon} a_\mathrm{s} \boldsymbol{u}_1$, where ρ_1 and $\boldsymbol{u}_1$ are time-dependent functions of $\mathcal{O}(1)$ that can be evaluated later. At the outset, one can write

$$\rho(x, y, t) = (\rho_\mathrm{s} + \rho_1^*)/\rho_\mathrm{s} = 1 + \bar{\varepsilon} \rho_1(x, y, t). \qquad (3.5)$$

In much the same way, velocity lends itself to decomposition. Knowing the mean solution from (2.1) and (2.2), we may follow Lighthill (1954) by assuming small velocity oscillations about the mean and expand the dimensional velocity as

$$\boldsymbol{u}^*(x^*, y^*, t^*) = \boldsymbol{u}_0^*(x^*, y^*) + \boldsymbol{u}_1^*(x^*, y^*, t^*) = v_\mathrm{w} \boldsymbol{u}_0(x^*, y^*) + \boldsymbol{u}_1^*(x^*, y^*, t^*). \qquad (3.6)$$

Normalizing by a_s begets, for the velocity and vorticity companion,

$$\boldsymbol{u}(x, y, t) = M \boldsymbol{u}_0(x, y) + \bar{\varepsilon} \boldsymbol{u}_1(x, y, t) \quad \text{and} \quad \boldsymbol{\omega}(x, y, t) = M \boldsymbol{\omega}_0(x, y) + \bar{\varepsilon} \boldsymbol{\omega}_1(x, y, t). \qquad (3.7)$$

(c) Linearization

Inserting (3.4)–(3.7) back into (3.1), (3.2) produces the zero-order expansion in the wave amplitude (which is already satisfied by the mean flow). Collecting terms of $\mathcal{O}(\bar{\varepsilon})$, the first-order linearized expansion of the fundamental equations is obtained:

$$\partial \rho_1/\partial t + \nabla \cdot \boldsymbol{u}_1 = -M \nabla \cdot (\rho_1 \boldsymbol{u}_0), \qquad (3.8)$$

$$\partial \boldsymbol{u}_1/\partial t = -M[\nabla(\boldsymbol{u}_0 \cdot \boldsymbol{u}_1) - \boldsymbol{u}_1 \times (\nabla \times \boldsymbol{u}_0) - \boldsymbol{u}_0 \times (\nabla \times \boldsymbol{u}_1)]$$
$$- \nabla p_1 + \bar{R}^{-1}[\tfrac{4}{3}\nabla(\nabla \cdot \boldsymbol{u}_1) - \nabla \times (\nabla \times \boldsymbol{u}_1)]. \qquad (3.9)$$

This set encapsulates the influence of bulk fluid motion on the temporal field. The reader unfamiliar with this set may, if so inclined, derive it straightforwardly or apply to the first author for a typescript.

4. Vector superposition

(a) Flow field decomposition

It is useful to decompose the time-dependent vector into an irrotational and a solenoidal component, the former being the gradient of a scalar s and the latter being the curl of a vector $\boldsymbol{q}$. This notion correlates to a known mathematical theorem which can be used to synthesize the total harmonic disturbance out of two components associated with irrotational, pressure-driven and solenoidal vorticity-driven modes. Using a hat to designate irrotational parts, and a tilde for solenoidal parts, the time-dependent velocity can be expressed as

$$\boldsymbol{u}_1 = \hat{\boldsymbol{u}} + \tilde{\boldsymbol{u}} \equiv \nabla s + \nabla \times \boldsymbol{q}. \tag{4.1}$$

Clearly, $\nabla \times \hat{\boldsymbol{u}} = \boldsymbol{0}$ and $\nabla \cdot \tilde{\boldsymbol{u}} = 0$. Similar decomposition of a small disturbance into pressure and vorticity modes has been effectuated previously by numerous authors, including Chu & Kovásznay (1957), Carrier & Carlson (1946) and others. It follows that

$$\boldsymbol{\omega}_1 \equiv \nabla \times \boldsymbol{u}_1 = \tilde{\boldsymbol{\omega}} \equiv \nabla \times \tilde{\boldsymbol{u}}, \quad p_1 = \hat{p} \quad \text{and} \quad \rho_1 = \hat{\rho}. \tag{4.2}$$

In other words, time-dependent vorticity is ascribed to the rotational mode and harmonic pressure is associated with the irrotational mode. The pseudo-pressure arising in the vortical mode analysis can be safely dismissed, being of second order. The last term in (4.2) stems from the known relation, $\hat{p} = \hat{\rho}$, for a perfect gas undergoing isentropic oscillations.

(b) Splitting the linearized Navier–Stokes equations

When (4.1), (4.2) are substituted back into (3.8), (3.9), two independent sets of formulae can be segregated. These are coupled through existing boundary conditions and are given by the following.

(i) *Irrotational set*

$$\frac{\partial \hat{\rho}}{\partial t} + \nabla \cdot \hat{\boldsymbol{u}} = -M \nabla \cdot (\hat{\rho} \boldsymbol{u}_0), \tag{4.3}$$

$$\frac{\partial \hat{\boldsymbol{u}}}{\partial t} = -\nabla \hat{p} - M[\nabla(\hat{\boldsymbol{u}} \cdot \boldsymbol{u}_0) - \hat{\boldsymbol{u}} \times (\nabla \times \boldsymbol{u}_0)] + \tfrac{4}{3} \bar{R}^{-1} \nabla(\nabla \cdot \hat{\boldsymbol{u}}). \tag{4.4}$$

(ii) *Solenoidal set*

$$\nabla \cdot \tilde{\boldsymbol{u}} = 0, \tag{4.5}$$

$$\frac{\partial \tilde{\boldsymbol{u}}}{\partial t} = -M[\nabla(\tilde{\boldsymbol{u}} \cdot \boldsymbol{u}_0) - \tilde{\boldsymbol{u}} \times (\nabla \times \boldsymbol{u}_0) - \boldsymbol{u}_0 \times (\nabla \times \tilde{\boldsymbol{u}})] - \bar{R}^{-1} \nabla \times (\nabla \times \tilde{\boldsymbol{u}}). \tag{4.6}$$

(c) Auxiliary conditions

In deriving $\boldsymbol{u}_1$, both $\hat{\boldsymbol{u}}$ and $\tilde{\boldsymbol{u}}$ must be first determined and then superposed in a manner to satisfy correctly two auxiliary conditions. These are (1) no slip at the wall demanding that $u_1(x, 0) = 0$, or $\hat{u}(x, 0) + \tilde{u}(x, 0) = 0$; and (2) symmetry at $y = 1$ requiring that $\partial u_1(x, 1)/\partial y = 0$.

(d) Irrotational solution

When $\hat{p} = \hat{\rho}$ is used, standard manipulation of (4.3), (4.4) condenses the set into a single hyperbolic partial differential equation:

$$\frac{\partial^2 \hat{p}}{\partial t^2} - \nabla^2 \hat{p} = -M \left\{ \nabla \cdot \left(\frac{\boldsymbol{u}_0 \partial \hat{p}}{\partial t} \right) - \nabla^2 (\hat{\boldsymbol{u}} \cdot \boldsymbol{u}_0) + \nabla \cdot [\hat{\boldsymbol{u}} \times (\nabla \times \boldsymbol{u}_0)] \right\}. \quad (4.7)$$

At this juncture, a solution can be managed at $\mathcal{O}(M)$ by applying separation of variables and the rigid wall boundary conditions. Since $l \gg 1$, the lowest naturally excited frequencies will correspond to the least damped longitudinal oscillation modes, making it safe to neglect transverse modes of higher frequencies. In practice, laboratory experiments confirm that low-frequency modes tend to dominate because they require less energy to become excited. For axial harmonic waves in a long channel with constant cross-section, a solution to (4.7) is readily available. Expressed in Euler's notation, the corresponding harmonic pressure component is

$$\hat{p}(x, t) = \cos(k_m x) \exp(-\mathrm{i} k_m t) + \mathcal{O}(M), \quad (4.8)$$

where the dimensionless wavenumber is given by

$$k_m = kh/a_\mathrm{s} = m\pi/l, \quad m = 1, 2, 3, \dots,$$

and m is the oscillation mode number. The velocity companion can be integrated from (4.4) to get

$$\hat{\boldsymbol{u}}(x, t) = \mathrm{i} \sin(k_m x) \exp(-\mathrm{i} k_m t) \boldsymbol{i} + \mathcal{O}(M). \quad (4.9)$$

(e) Solenoidal equations

Letting $\bar{\boldsymbol{u}}(x, y) \equiv \bar{u} \boldsymbol{i} + \bar{v} \boldsymbol{j}$, and $\bar{\boldsymbol{\omega}}(x, y) \equiv \nabla \times \bar{\boldsymbol{u}} = \bar{\omega} \boldsymbol{k}$, we use Euler's notation and write the vortical fluctuations as

$$\tilde{\boldsymbol{u}}(x, y, t) = \bar{\boldsymbol{u}}(x, y) \exp(-\mathrm{i} k_m t), \quad \tilde{\boldsymbol{\omega}}(x, y, t) = \bar{\boldsymbol{\omega}}(x, y) \exp(-\mathrm{i} k_m t). \quad (4.10)$$

In lieu of (4.5) and (4.6), we now have

$$\nabla \cdot \bar{\boldsymbol{u}} = 0, \quad (4.11)$$

$$\mathrm{i} \bar{\boldsymbol{u}} = [\nabla(\bar{\boldsymbol{u}} \cdot \boldsymbol{u}_0) - \bar{\boldsymbol{u}} \times \boldsymbol{\omega}_0 - \boldsymbol{u}_0 \times \bar{\boldsymbol{\omega}}]/S + \nabla \times \bar{\boldsymbol{\omega}}/K, \quad (4.12)$$

where

$$S = \frac{kh}{v_\mathrm{w}} \quad \text{and} \quad K = \frac{kh^2}{\nu} = \frac{h^2}{(\sqrt{\nu/k})^2}. \quad (4.13)$$

The two emerging similarity parameters are the Strouhal number S and the kinetic Reynolds number K, each representing the quotient of time-dependent inertia to either mean flow convection or diffusion. Practically, since the kinematic viscosity of most gases happens to be very small, the parametric variation in K reported by many researchers has fallen into the range $10^4 < K < 10^8$. On that account, we define $\varepsilon \equiv 1/K$ to be a primary perturbation parameter. For similar reasons, since unsteady flows are characterized by appreciable Strouhal numbers, we define $\sigma = 1/S$. We note that ε is always smaller than σ since the ratio $\sigma/\varepsilon = v_\mathrm{w} h/\nu$ is the cross-flow Reynolds number R, which is typically large irrespective of frequency.

Subject to confirmation at the conclusion of the forthcoming analysis, we now make the conditional stipulation that $\bar{v}/\bar{u} = \mathcal{O}(M)$. This proviso is necessary to forge ahead with the leading-order approximation. Being a smaller quantity, $\bar{v}$ can be omitted at the first perturbation level. On that account, (4.12) collapses at $\mathcal{O}(M)$ into

$$\mathrm{i}\bar{u} = \sigma\left[\frac{\partial}{\partial x}(\bar{u}u_0) + v_0\frac{\partial\bar{u}}{\partial y}\right] - \varepsilon\frac{\partial^2\bar{u}}{\partial y^2} \quad \text{or} \quad \mathrm{i}\bar{u} = \sigma\left[\frac{\partial}{\partial x}(\bar{u}u_0) - v_0\bar{\omega}\right] + \varepsilon\frac{\partial\bar{\omega}}{\partial y}. \quad (4.14)$$

5. Vorticity transport formulation

(a) Vorticity transport equation

Taking the curl of (4.12) and using (4.10), the vorticity transport equation emerges:

$$\mathrm{i}\bar{\boldsymbol{\omega}} = -\sigma\nabla \times (\bar{\boldsymbol{u}} \times \boldsymbol{\omega}_0 + \boldsymbol{u}_0 \times \bar{\boldsymbol{\omega}}) - \varepsilon\nabla^2\bar{\boldsymbol{\omega}} + \mathcal{O}(M). \quad (5.1)$$

This can be rearranged in a scalar form that places leading-order terms on the left-hand side:

$$\frac{\partial\bar{\omega}}{\partial y} - \frac{\mathrm{i}\bar{\omega}}{\sigma v_0} + \frac{u_0}{v_0}\frac{\partial\bar{\omega}}{\partial x} = -\frac{\bar{u}}{v_0}\frac{\partial\omega_0}{\partial x} + \frac{\varepsilon}{\sigma v_0}\left(\frac{\partial^2\bar{\omega}}{\partial x^2} + \frac{\partial^2\bar{\omega}}{\partial y^2}\right). \quad (5.2)$$

The right-hand side quantities representing the steady vorticity gradient and the viscous diffusion of time-dependent vorticity can be ignored at the first perturbation level. The base solution can now be achieved by expanding $\bar{\omega}$ in powers of M, namely $\bar{\omega} = \varpi_0 + M\varpi_1 + \mathcal{O}(M^2)$. Following substitution into (5.2), the leading-order term can be obtained, by separation of variables, from

$$\frac{\partial\varpi_0}{\partial y} - \frac{\mathrm{i}\varpi_0}{\sigma v_0} + \frac{u_0}{v_0}\frac{\partial\varpi_0}{\partial x} = 0. \quad (5.3)$$

This, of course, must be contingent upon satisfaction of both the no-slip condition at the wall, and the no-flow restriction at the head end. Using $\varpi_0 = X(x)Y(y)$ in (5.3), integration gives

$$\varpi_0(x, y) = \sum_{\lambda_n} c_n[x\cos(\tfrac{1}{2}\pi y)]^{\lambda_n} \exp\left\{\frac{2\mathrm{i}}{\pi\sigma}\ln\tan[\tfrac{1}{4}\pi(1+y)]\right\}, \quad (5.4)$$

where ϖ_0 contains a denumerable set of arbitrary constants c_n associated with each λ_n. Here λ_n must be a positive number for a non-trivial solution. Both c_n and λ_n must be specified in a manner to satisfy the no-slip condition at the wall, written for vorticity. The latter requires a delicate treatment and is addressed separately.

(b) Pressure-driven vorticity

Recalling that $\omega_1 = \tilde{\omega}$, $v_1 = \tilde{v}$, $p_1 = \hat{p}$ and that $u_1(x, 0, t)$ must vanish to prevent slippage, (3.9) can be projected along x and evaluated at the wall. The result is

$$0 = -M\left[\frac{\partial}{\partial x}(\tilde{v}v_0) - \tilde{v}\omega_0 - v_0\tilde{\omega}\right] - \frac{\partial\hat{p}}{\partial x} - \frac{1}{R}\frac{\partial\tilde{\omega}}{\partial y}. \quad (5.5)$$

Rearranging, and using the fact that the no-slip condition translates into

$$\tilde{\omega} = \frac{1}{M}\frac{\partial \hat{p}}{\partial x} + \frac{\varepsilon}{\sigma}\frac{\partial \tilde{\omega}}{\partial y} + \frac{\partial \tilde{v}}{\partial x} + \tfrac{1}{4}\pi^2 x\tilde{v} = -S\sin(k_m x)\exp(-ik_m t) + \frac{1}{R}\frac{\partial \tilde{\omega}}{\partial y} + \mathcal{O}(M),$$

(5.6)

one obtains

$$\bar{\omega}(x,0) = -S\sin(k_m x) + \frac{1}{R}\frac{\partial \bar{\omega}}{\partial y} + \mathcal{O}(M).$$

(5.7)

Equation (5.7) indicates that 'fresh' vorticity owes its origin at the wall to the oscillatory pressure gradient that is at right angles to incoming fluxes. We also realize that vorticity is most intense at $x/l = (2m - 1)/(2m)$, coinciding with pressure nodes where the pressure-induced $\hat{u}$ has maximum amplitude. By comparison with the pressure, time-dependent vorticity is larger by $\mathcal{O}(S)$.

(c) *Inviscid vorticity*

Equation (5.7) can now be used in conjunction with (5.4) to specify the separation eigenvalues:

$$\varpi_0(x,0) = -S\sin(k_m x) + \mathcal{O}(M, R^{-1}) \equiv -S\sum_{n=0}^{\infty}\frac{(-1)^n(k_m x)^{2n+1}}{(2n+1)!},$$

(5.8)

$$\Rightarrow \lambda_n = 2n+1 \quad \text{and} \quad c_n = -S(-1)^n(k_m)^{2n+1}/(2n+1)!,$$

(5.9)

whence

$$\varpi_0(x,y) = S\left\{\sum_{n=0}^{\infty}\frac{(-1)^n}{(2n+1)!}[-k_m x\cos(\tfrac{1}{2}\pi y)]^{2n+1}\right\}\exp\left\{\frac{2}{\pi}iS\ln\tan[\tfrac{1}{4}\pi(1+y)]\right\}.$$

(5.10)

Recalling Taylor's mean flow stream function from §2 *c*, we recognize that the infinite series between braces is a sine function of Ψ. At the outset, we let $Z(x,y) \equiv k_m\Psi(x,y)$ and simplify (5.10) into

$$\varpi_0(x,y) = S\sin(Z)\exp(-i\Phi_0),$$

(5.11)

where the temporal phase lead of the vortical wave is found to depend on

$$\Phi_0(y) = -\frac{2}{\pi}S\ln\tan[\tfrac{1}{4}\pi(1+y)] = -\frac{2}{\pi}S\,\mathrm{gd}^{-1}(\tfrac{1}{2}\pi y).$$

(5.12)

The last expression corresponds to $\mathrm{gd}(\varsigma) = 2\arctan(\varsigma) - \tfrac{1}{2}\pi$, the Gudermannian function described in Abramowitz & Stegun (1964).

(d) *Inviscid stream function*

We now resort to the time-dependent stream function $\bar{s} = \psi k$, where $\bar{u} \equiv \nabla \times \bar{s}$. These expressions are used to replace the velocity components via $\bar{u} = \partial\psi/\partial y$ and $\bar{v} = -\partial\psi/\partial x$. Starting with

$$\bar{\omega} = \frac{\partial \bar{v}}{\partial x} - \frac{\partial \bar{u}}{\partial y} = -\frac{\partial^2 \psi}{\partial x^2} - \frac{\partial^2 \psi}{\partial y^2},$$

(5.13)

we then proceed heuristically by posing that ψ must possess the same axial dependence as $\bar{\omega}$. Since we are using successive approximations, we set $\psi_0 = \psi_c \varpi_0$, and substitute back into (5.13). Balancing leading-order terms implies

$$\psi_c = \sigma^2 \cos^2(\tfrac{1}{2}\pi y) \quad \text{or} \quad \psi_0 = \sigma \cos^2(\tfrac{1}{2}\pi y) \sin[-k_m x \cos(\tfrac{1}{2}\pi y)] \exp(-i\Phi_0). \quad (5.14)$$

Having determined the inviscid flow stream function, it follows that the companion velocity is

$$\bar{u}(x,y) = [i\cos(\tfrac{1}{2}\pi y)\sin(Z)\boldsymbol{i} + M\cos^3(\tfrac{1}{2}\pi y)\cos(Z)\boldsymbol{j}]\exp(-i\Phi_0). \quad (5.15)$$

(e) Viscous corrections

Subject to verification at the conclusion of this section, we state without proof that both $\bar{u}$ and $\bar{\omega}$ must possess the same axial dependence as their inviscid counterparts. This is implemented by setting

$$\bar{u}(x,y) = u_c(y)\sin(Z)\exp(-i\Phi_0) \quad \text{and} \quad \bar{\omega}(x,y) = \varpi_c(y)\sin(Z)\exp(-i\Phi_0), \quad (5.16)$$

where viscous correction multipliers, u_c and ϖ_c, must be evaluated. After substitution into the full vorticity transport equation, given by (5.2), several terms cancel out except for lower-order terms and terms of $\mathcal{O}(S^2)$. Balancing leading-order terms requires that

$$\mathrm{d}\varpi_c/\mathrm{d}y + \xi\sec^3(\tfrac{1}{2}\pi y)\varpi_c - \tfrac{1}{4}\pi^2 u_c = 0, \quad (5.17)$$

where $\xi = k_m^2/(M^3\bar{R})$ appears as a dynamic similarity parameter, chiefly in control of the viscous correction multiplier. In seeking a relationship between u_c and ϖ_c, we use (4.14) and find that

$$u_c = [i\sigma\cos(\tfrac{1}{2}\pi y) + \xi\sigma^2\sec(\tfrac{1}{2}\pi y)]\varpi_c. \quad (5.18)$$

Inserting this formula into (5.17) leads to an ordinary differential equation in ϖ_c:

$$\mathrm{d}\varpi_c/\mathrm{d}y + [\xi\sec^3(\tfrac{1}{2}\pi y) - i\sigma\tfrac{1}{4}\pi^2\cos(\tfrac{1}{2}\pi y)]\varpi_c = 0, \quad (5.19)$$

which, after some algebra, gives

$$\varpi_c(y) = C\exp\zeta, \quad (5.20)$$

where, by omitting the imaginary argument in ζ of effective $\mathcal{O}(\sigma^2)$, we find

$$\zeta = -\xi\int_0^y v_0^{-3}(\tau)\,\mathrm{d}\tau = -\xi\int_0^y F^{-3}(\tau)\,\mathrm{d}\tau$$

$$= -\frac{1}{\pi}\xi[\ln\tan\tfrac{1}{4}\pi(1+y) + \sec(\tfrac{1}{2}\pi y)\tan(\tfrac{1}{2}\pi y)]. \quad (5.21)$$

(f) Corrected vorticity

The complex constant of integration C can be evaluated from the vorticity boundary condition at the wall as specified by (5.7). Updating ϖ_c gives, at $\mathcal{O}(M,\sigma^2)$,

$$C\{1 - \xi\sigma^2[\zeta'(0) - i\Phi_0'(0)]\}\sin[Z(x,0)]\exp[\zeta(0) - i\Phi_0(0)] = -S\sin(k_m x), \quad (5.22)$$

where

$$\zeta'(0) = -\xi, \quad \Phi_0'(0) = -S \quad \text{and} \quad \zeta(0) = \Phi_0(0) = 0. \tag{5.23}$$

Direct substitution gives

$$C^{\mathrm{r}} = S^3/(S^2 + \xi^2), \quad C^{\mathrm{i}} = \xi S^2/(S^2 + \xi^2). \tag{5.24}$$

The superscripts here designate real and imaginary parts. Backward substitution into (5.20), (5.16) and (4.10) yields

$$\tilde{\omega}(x, y, t) = C \sin(Z) \exp(\zeta - \mathrm{i}\Phi_0 - \mathrm{i}k_m t). \tag{5.25}$$

(g) Corrected axial velocity

In much the same way, the velocity corrective multiplier can be deduced from (5.18), namely

$$u_{\mathrm{c}} = [\mathrm{i}\sigma \cos(\tfrac{1}{2}\pi y) + \xi\sigma^2 \sec(\tfrac{1}{2}\pi y)]C \exp\zeta \equiv \mathrm{i}B \exp\zeta, \tag{5.26}$$

where

$$B^{\mathrm{r}} = \sigma(C^{\mathrm{r}}v_0 + \xi\sigma C^{\mathrm{i}}/v_0), \quad B^{\mathrm{i}} = \sigma(C^{\mathrm{i}}v_0 - \xi\sigma C^{\mathrm{r}}/v_0) \tag{5.27}$$

so that $\tilde{\boldsymbol{u}}$ is soluble by backward substitution into (5.16) and (4.10). At length, we find that

$$\tilde{u}(x, y, t) = \bar{u}\exp(-\mathrm{i}k_m t) = \mathrm{i}B \sin(Z) \exp(\zeta - \mathrm{i}\Phi_0 - \mathrm{i}k_m t). \tag{5.28}$$

(h) Normal velocity

In principle, the normal component $\tilde{v}$ can be derived from continuity. In practice, this may prove difficult unless we proceed heuristically by first proposing an ansatz of the form

$$\tilde{v} = g(y) \cos[-k_m x \cos(\tfrac{1}{2}\pi y)] \exp(\zeta - \mathrm{i}\Phi_0 - \mathrm{i}k_m t). \tag{5.29}$$

Later substitution into (4.5) furnishes $g(y)$. Setting $\partial\tilde{v}/\partial y \equiv -\partial\tilde{u}/\partial x$, we find, to leading order, $g = MBv_0^2$. Therefore,

$$\tilde{v}(x, y, t) = MBv_0^2 \cos(Z) \exp(\zeta - \mathrm{i}\Phi_0 - \mathrm{i}k_m t), \tag{5.30}$$

which lends support to the former stipulation contending that $\tilde{v}/\tilde{u} = \mathcal{O}(M)$.

(i) The real time-dependent solution

Retracing our steps, the meaningful components of time-dependent axial and normal velocity are recapitulated along with their vorticity companion as follows:

$$u_1 = \sin(k_m x) \sin(k_m t) - (B^{\mathrm{r}} \sin\varphi - B^{\mathrm{i}} \cos\varphi) \exp\zeta \sin(k_m x \cos\theta), \tag{5.31}$$

$$v_1 = -Mv_0^2(B^{\mathrm{r}} \cos\varphi + B^{\mathrm{i}} \sin\varphi) \exp\zeta \cos(k_m x \cos\theta), \tag{5.32}$$

$$\omega_1 = -(C^{\mathrm{r}} \cos\varphi + C^{\mathrm{i}} \sin\varphi) \exp\zeta \sin(k_m x \cos\theta), \tag{5.33}$$
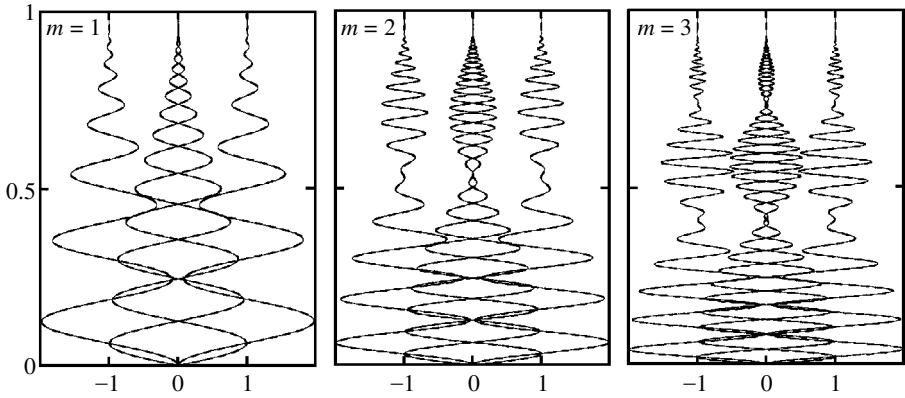
Figure 2. A plot of u_1 versus y at four successive times separated by a $\pi/2$ phase difference. For every oscillation mode, profiles are depicted at the last harmonic pressure node, where $x/l = (2m-1)/2m$. Here $S = 25m$ and $K = 10^6 m$. To the accuracy of the graph, asymptotics (full lines) and numerics (broken lines) are indistinguishable.

where

$$\theta = \tfrac{1}{2}\pi y \quad \text{and} \quad \varphi = k_m t - \frac{2}{\pi} S \ln \tan(\tfrac{1}{4}\pi + \tfrac{1}{2}\theta). \tag{5.34}$$

As the harmonic motion is driven by the oscillatory pressure field, the first term in (5.31) can be envisaged as the inviscid response to the fluctuating pressure. Likewise, the second term can be interpreted as the viscous and vortical response that disappears asymptotically with increasing distance from the wall.

6. Vortical wave character

(a) Numerical verification

In order to gain confidence in the asymptotic formulae based on (5.31), we rely on computer-generated numerics and numerics combined with physical arguments. To that end, we use a shooting method to handle the two-point boundary-value problem posing itself via (4.14) and the two auxiliary conditions described in § 4 c. Careful choices of initial guesses are found to be necessary to ensure convergence. Our preference is to guess small non-zero values at the core and integrate backwards using a seventh-order Runge–Kutta scheme until the no-slip condition at the wall is satisfied. Uniform steps, albeit very minute ones because of the desired accuracy, are found to be adequate for the most part. If the spatial grid is too coarse, then a numerical overflow occurs. Naturally, the numerical difficulty arises at large kinetic Reynolds numbers. Continual spatial grid refinement is hence necessary at successive increases in K. The number of grid points needed for convergence varied in our monitored routine from 10 000 to 20 000 000 points, but no effort was made to optimize the number by employing non-uniform meshes.

For typical values of the control parameters, the velocity's numerical solution is compared in figure 2 with its asymptotic counterpart evaluated from (5.31). For the first three oscillation modes, profiles are shown at four selected times of a complete cycle. For the fundamental mode, u_1 starts at zero at the wall, in satisfaction of the
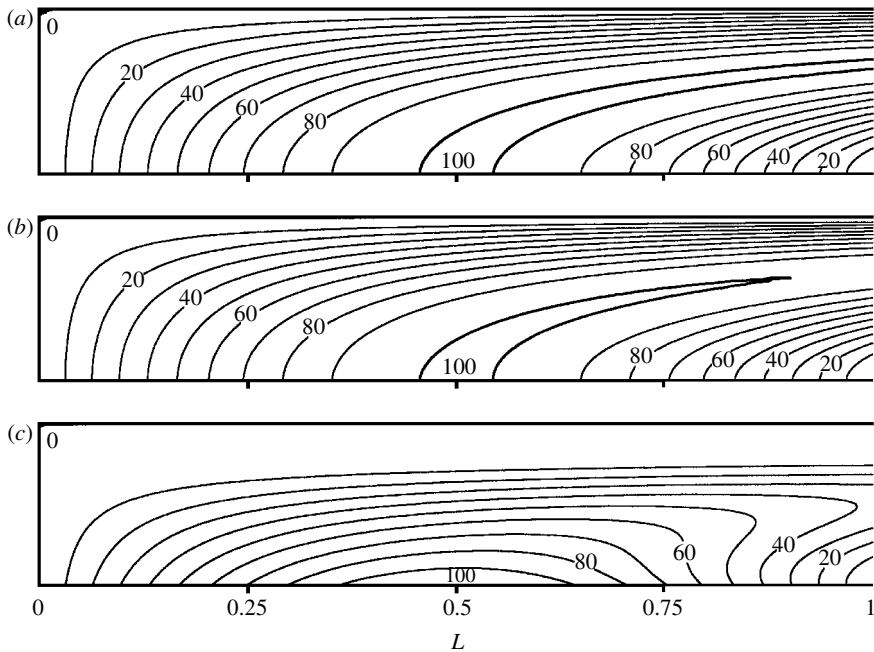
Figure 3. Evenly spaced iso-vorticity lines shown in (a), (b) and (c) for $S = 10$, 20 and 100. In each case, $m = 1$ and $K = 10^6 m$. This variation can be ascribed to an order of magnitude depreciation in wall injection.

no-slip condition, then undergoes a velocity overshoot of twice the irrotational core amplitude, before decaying gradually to its inviscid form. This overshoot near the wall is a well-known feature of oscillatory flows that was first reported by Richardson (1928). The observed doubling in amplitude takes place when rotational and irrotational waves happen to be in phase. This virtual 100% amplification is far more intense than the 13% overshoot described in Rott (1964, p. 402) and reported in laboratory experiments conducted, in the absence of wall injection, by Richardson (1928) and Richardson & Tyler (1929).

For higher modes, similar damped waves are observed for $0 < x/l < 1/m$ in the upstream portion that is delimited by the first internal velocity node. In the downstream portion, additional structures emerge. Specifically, a premature decay in the rotational wave is noted $m - 1$ times downstream of the mth velocity node. Such structures are depicted in figure 2 for $m = 2$ and 3, at the last pressure node where irrotational velocity amplitudes are largest. Beyond these premature rotational velocity 'nodes', so to speak, the vortical field recuperates some strength before resuming its normal depreciation. In order to justify the presence of such intellectually challenging rotational nodes, a characterization of the time-dependent vortical structure is deemed necessary. In the process, the influence of varying wall injection and kinematic viscosity is captured.

(b) Time-dependent vortical structure

For $m = 1$, (5.33) can be used to generate contour plots showing constant vorticity lines in per cent of the maximum vorticity amplitude that is produced at the
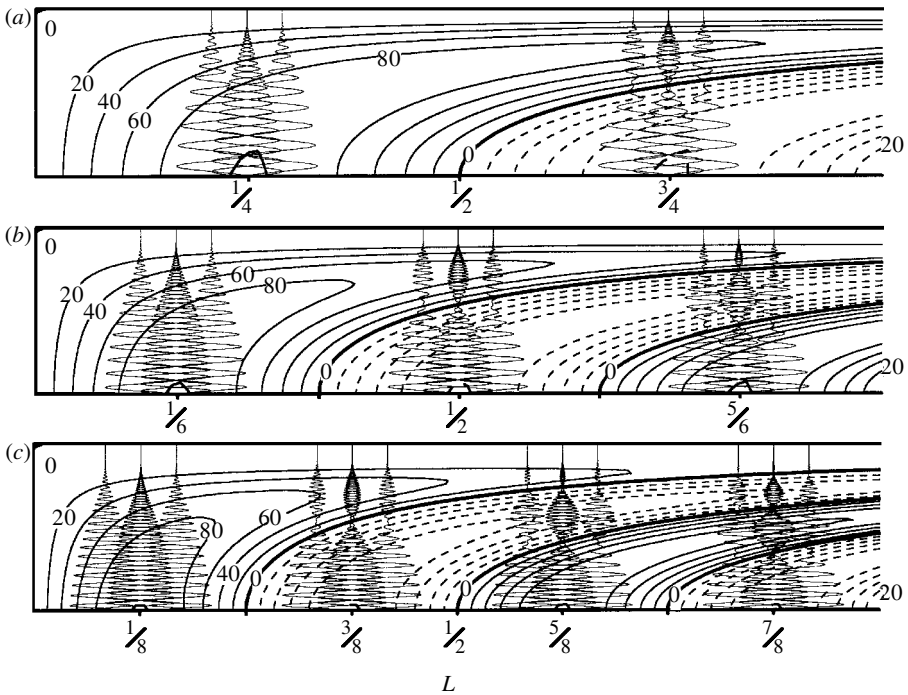
Figure 4. Evenly spaced iso-vorticity lines shown in (a), (b) and (c) for the first three harmonics when $S = 25m$ and $K = 10^6 m$. The oscillatory velocity u_1 is abbreviated by four evenly spread timelines depicted at select locations coinciding with harmonic pressure nodes.

wall's pressure nodes. When the frequency and kinematic viscosity are held constant, corresponding to a typical $K = 10^6$ value, the Strouhal number can be modified by an order of magnitude by reducing the injection rate. The corresponding vortical structures are shown in figure 3, for $S = 10$, 20 and 100. In particular, we note in figure 3a the deeper vortical penetration with higher injection, and the downstream convection of vorticity, originating at the wall, that follows the mean flow stream-lines. In figure 3a, b, intense vorticity is still present at the downstream end measuring close to 100% of its maximum generated at the wall. When injection is diminished in figure 3c, the irrotational region anchored at the core broadens out, resulting in a substantial reduction in rotational depth. When this happens, intense vortical waves are entrained in the vicinity of the wall, and only weak vorticity persists at the downstream end.

When, instead, v_w and k are held constant, the effect of kinematic viscosity can be extrapolated in a similar fashion by varying K. We find that, when viscosity is suppressed, a wider and deeper spread of vorticity ensues. As such, one can envisage viscosity as an attenuation agent whose role is to resist the propagation of rotational waves. This is contrary to the role it plays in similar configurations with impermeable walls discussed, for example, in a survey by Rott (1964, p. 397).

As the oscillation mode evolves to $m = 2$, 3 and 4, isovorticity lines begin exhibiting interesting structures. These are shown in figure 4 for typical values of the control parameters. In particular, these structures feature $(m - 1)$ lines of zero-vorticity amplitude, stemming from the harmonic pressure antinodes at the wall, for $m > 1$.
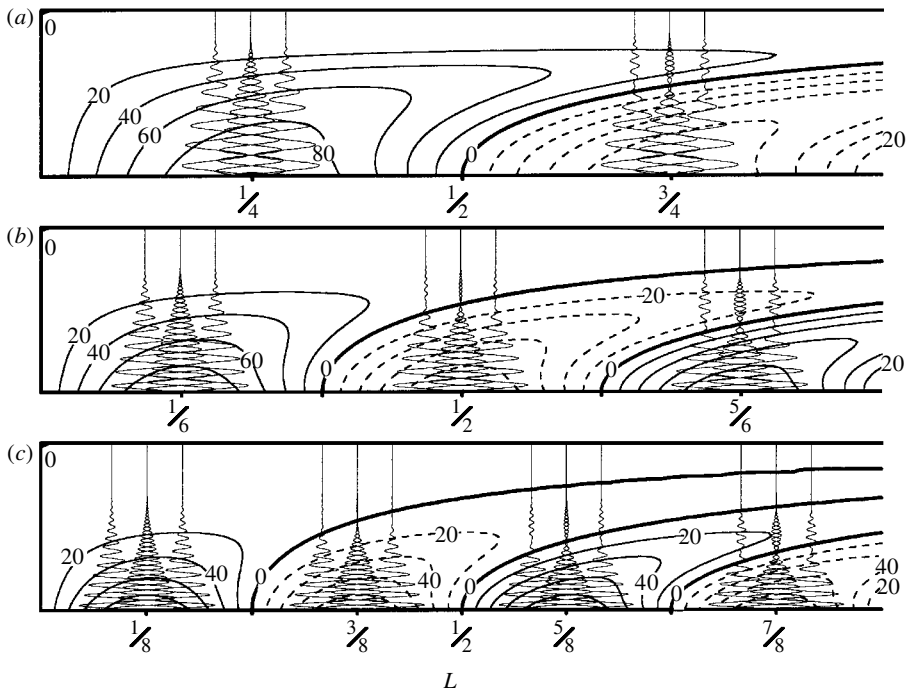
Figure 5. As in figure 4, unsteady velocity profiles overlay evenly spaced iso-vorticity lines in (a), (b) and (c) for the first three harmonics. Here $K = 10^5 m$, corresponding to an order of magnitude increase in kinematic viscosity. In the presence of surface injection, the penetration of rotationality is inhibited by viscous dissipation.

These irrotational streaks partition the channel into m zones characterized by alternating directions of particle rotation. When crossing these delineation lines, vorticity changes sign and therefore direction. This effect is captured graphically by switching between zones from full lines to broken lines. When time-dependent velocity profiles are superimposed at select axial locations, we find that the so-called rotational nodes in u_1 coincide precisely with the transverse location of the zero vorticity streaks. Similar effects are noted in figure 5, where an order of magnitude increase in viscosity is shown to reduce both vortical wave propagation depth and also amplitude at higher modes.

(c) *Limiting process verification*

In order to establish the lower limit that our mathematical model can tolerate for injection speeds, we reduce v_w until it drops below the diffusion speed, $v_d = \sqrt{2k\nu}$. The latter is associated with a Stokes oscillatory field in a channel bounded by impermeable walls. This is necessitated by the insoluble singularity at $v_w = 0$ in our formulation. For example, when $v_w = v_d/\sqrt[3]{2}$, corresponding to $S = \sqrt{(K/\sqrt[3]{2})}$, and $R = 2^{1/6}h\sqrt{(k/\nu)}$, the Stokes number, defined here as $\lambda_S = \sqrt{(K/2)}$, will match the viscous parameter $\xi = S^3/K$. When such conditions are established ($\xi = \lambda_S$), our asymptotic formulation can be compared with the known exact solution found, for example, in Rott (1964, p. 402). The latter corresponds to an oscillatory
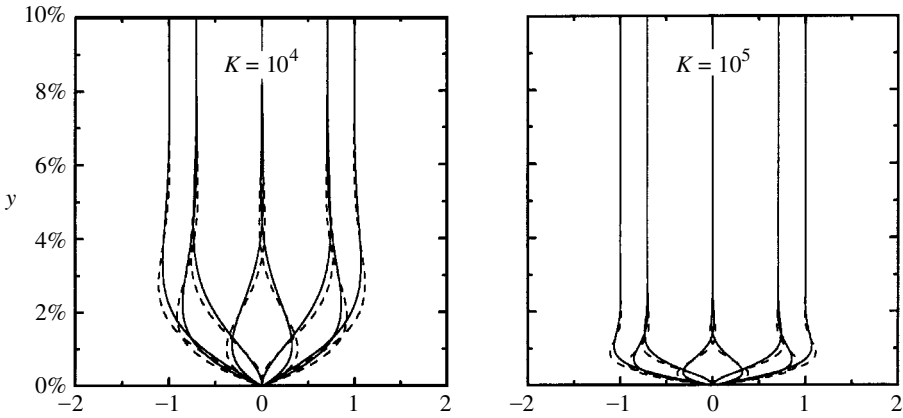
Figure 6. Velocity profiles of u_1 shown at eight successive time intervals. Results are obtained from asymptotic predictions (broken lines) and the exact Stokes formula (full lines) at two arbitrary values of K and $\xi = \lambda_S$. In the absence of surface injection, the penetration of rotationality is more pronounced at higher viscosity settings (left).

flow in an infinitely long impermeable channel that is not tailored to accommodate either variations in the streamwise direction, or oscillation modes brought about by the finite geometry. As such, it maintains a constant core amplitude. In order to reproduce this condition caused by 'pistons-at-infinity', we compare solutions at $x/l = \frac{1}{2}$ and $m = 1$, where the effects of finite body-length are not felt. Results are shown in figure 6 at eight successive times separated by a $\frac{1}{4}\pi$ phase difference. Apparently, our approximate solution embraces the exact solution when injection is suppressed. Thus, although it is possible to approximate the impermeable channel solution from ours, the converse is not true. This unexpected result may be attributed to the fact that Taylor's mean flow solution matches, near the wall, the more accurate formulation derived by Berman (1953) for small injection. In our notation, the latter is given by

$$F = 1 - \tfrac{3}{2}y^2 + \tfrac{1}{2}y^3,$$

which resembles, near $y = 0$, Taylor's

$$F = \cos(\tfrac{1}{2}\pi y) = 1 - \tfrac{1}{8}\pi^2 y^2 + \mathcal{O}(y^4).$$

7. Momentum transport formulation

(a) Separation of variables

In §5, the rotational velocity was produced from the vorticity and vorticity transport equations following a number of successive approximations. Here, $\tilde{u}$ will be obtained directly from the momentum equation, written to $\mathcal{O}(M)$. To that end, we rearrange (4.14) into

$$x\frac{\partial\bar{u}}{\partial x} = \frac{2}{\pi}S\cosec(\tfrac{1}{2}\pi y)\left\{[\mathrm{i} - \tfrac{1}{2}\pi\sigma\sin(\tfrac{1}{2}\pi y)]\bar{u} - \sigma\cos(\tfrac{1}{2}\pi y)\frac{\partial\bar{u}}{\partial y} + \varepsilon\frac{\partial^2\bar{u}}{\partial y^2}\right\} + \mathcal{O}(M). \tag{7.1}$$

We then call for separation of variables in order to investigate a solution of the type $\bar{u}(x, y) = X(x)Y(y)$. Inserting back into (7.1) renders

$$\frac{x}{X}\frac{\mathrm{d}X}{\mathrm{d}x} = \frac{2S}{\pi Y}\mathrm{cosec}(\tfrac{1}{2}\pi y)\left\{[\mathrm{i} - \tfrac{1}{2}\pi\sigma\sin(\tfrac{1}{2}\pi y)]Y - \sigma\cos(\tfrac{1}{2}\pi y)\frac{\mathrm{d}Y}{\mathrm{d}y} + \varepsilon\frac{\mathrm{d}^2 Y}{\mathrm{d}y^2}\right\} = \lambda_n, \tag{7.2}$$

where λ_n must be strictly positive. Integration of the axially dependent equation is straightforward. Owing to the linearity of (7.1), the general solution takes the form

$$\bar{u}(x, y) = \sum_{\lambda_n} c_n x^{\lambda_n} Y_n(y), \tag{7.3}$$

where c_n is a simple integration constant, and λ_n must be determined from the no-slip boundary condition at the wall. The latter can be translated into $\tilde{u} = -\hat{u}$, or

$$\bar{u}(x, 0) = -\mathrm{i}\sin(k_m x). \tag{7.4}$$

After inserting (7.4) into (7.3), the Taylor series expansion for the sine function can be written out to get

$$\sum_{\lambda_n} c_n x^{\lambda_n} Y_n(0) \equiv -\mathrm{i}\sum_{n=0}^{\infty} \frac{(-1)^n (k_m x)^{2n+1}}{(2n+1)!}, \tag{7.5}$$

which is true when

$$\lambda_n = 2n + 1, \quad n = 0, 1, 2, \ldots, \quad c_n = -\mathrm{i}\frac{(-1)^n (k_m)^{2n+1}}{(2n+1)!}, \tag{7.6}$$

$$Y_n(0) = 1, \tag{7.7}$$

turning (7.3) into

$$\bar{u}(x, y) = -\mathrm{i}\sum_{n=0}^{\infty} \frac{(-1)^n (k_m x)^{2n+1}}{(2n+1)!} Y_n(y). \tag{7.8}$$

From (7.2), the velocity eigenfunction Y_n is left to be determined from

$$\varepsilon\frac{\mathrm{d}^2 Y_n}{\mathrm{d}y^2} - \sigma\cos(\tfrac{1}{2}\pi y)\frac{\mathrm{d}Y_n}{\mathrm{d}y} + [\mathrm{i} - \tfrac{1}{2}\pi\sigma(1 + \lambda_n)\sin(\tfrac{1}{2}\pi y)]Y_n = 0, \tag{7.9}$$

which must satisfy the two existing boundary conditions:

$$Y_n(0) = 1 \text{ (no-slip condition)} \quad \text{and} \quad \frac{\mathrm{d}Y_n(1)}{\mathrm{d}y} = 0 \text{ (core symmetry)}. \tag{7.10}$$

Due to the variable coefficients in (7.9), an exact closed-form solution is not feasible. The presence of a small multiplier in the highest derivative suggests, however, the possibility of a perturbation treatment. Knowing from §6 that the solution exhibits an oscillatory behaviour, both WKB and multiple-scale expansion methods may be attempted. In fact, the latter technique has been shown by Majdalani (1998) to result in partly valid solutions corresponding to outer, inner and intermediate scales. In the same work, a uniform two-scale expansion was presented using a hybrid technique. The technique was based on the choice of a composite scale that reproduced the inner, outer and intermediate scales in their respective domains. Instead of constructing the composite scale from our foreknowledge of scaling structures, we consider here a different avenue to determine the necessary scaling transformation.

(b) The WKB approach

The problem set out in (7.9), (7.10) contains two small perturbation parameters, ε and σ. Note that, since $\sigma/\varepsilon = R$, we are interested in cases for which $\varepsilon \to 0$ for fixed σ. As such, two cases may arise depending on the order of the Strouhal number.

(i) The outer expansion

For small Strouhal numbers, $\sigma = \mathcal{O}(1)$, and the leading-order term of the outer solution Y_n^o can be obtained from

$$-\sigma\cos(\tfrac{1}{2}\pi y)\frac{\mathrm{d}Y_n^o}{\mathrm{d}y} + [\mathrm{i} - \tfrac{1}{2}\pi\sigma(1+\lambda_n)\sin(\tfrac{1}{2}\pi y)]Y_n^o = 0. \qquad (7.11)$$

Fulfilment of $Y_n(0) = 1$ gives

$$Y_n^o = [\cos(\tfrac{1}{2}\pi y)]^{\lambda_n+1}\exp\left\{\frac{2}{\pi}\mathrm{i}S\ln\tan[\tfrac{1}{4}\pi(1+y)]\right\} \equiv (\cos\theta)^{2n+2}\exp\left(\frac{2}{\pi}\mathrm{i}S\,\mathrm{gd}^{-1}\theta\right). \qquad (7.12)$$

On the one hand, since the cosine factor in Y_n^o decays rapidly as $y \to 1$, the boundary condition at the core is satisfied by the first derivative. This eliminates the need for an inner solution at this order. On the other hand, the exponential term in Y_n^o denotes an oscillatory behaviour that is commensurate with the size of S. Since S can be large, the limitation of this regular perturbation approach becomes apparent when the first-order correction is evaluated. In fact, the resulting outer solution, at $\mathcal{O}(\varepsilon^2)$, is

$$Y_n^o = (\cos\theta)^{2n+2}\exp\left(\frac{2}{\pi}\mathrm{i}S\,\mathrm{gd}^{-1}\theta\right)$$
$$\times\left(1 - \varepsilon S\left\{\frac{1}{\pi}S^2(\mathrm{gd}^{-1}\theta + \sec\theta\tan\theta) + \pi(n+1)\,\mathrm{gd}^{-1}\theta - \pi(n+1)(2n+\tfrac{1}{2})\right.\right.$$
$$\times\left.\left.[\sec\theta\tan\theta + \ln\cos\theta - \ln(1-\sin\theta)] + \mathrm{i}S(2n+\tfrac{3}{2})\tan^2\theta\right\}\right). \qquad (7.13)$$

Due to the $\mathcal{O}(\varepsilon S^3)$ term in (7.13), a secular behaviour can be expected at large S. Since oscillations often occur at $S > 10$, a WKB analysis is certainly more suitable.

(ii) The WKB expansion

For large Strouhal numbers, $\sigma \ll 1$, and rapid oscillations occur on a short scale while a slow drift takes place on the scale $x = \mathcal{O}(1)$. The WKB ansatz can be formulated from

$$-\cos(\tfrac{1}{2}\pi y)Y_n' + \mathrm{i}SY_n = 0, \quad Y_n(0) = 1 \quad \text{or} \quad Y_n = \exp\left(\frac{2}{\pi}\mathrm{i}S\,\mathrm{gd}^{-1}\theta\right). \qquad (7.14)$$

Setting $Y_n = g(y)\exp[(2/\pi)\mathrm{i}S\,\mathrm{gd}^{-1}\theta]$ and substituting back into (7.9) gives

$$g' + [\varepsilon S^3\cos^{-3}\theta + \pi(n+1)\tan\theta]g = \mathcal{O}(\varepsilon S^2). \qquad (7.15)$$

The leading-order WKB formulation, at $\mathcal{O}(\varepsilon S^2)$, can be obtained therefrom:

$$Y_n^0 = (\cos\theta)^{2n+2}\exp(\zeta_0 - \mathrm{i}\Phi_0), \quad \zeta_0 = -\frac{1}{\pi}\xi(\mathrm{gd}^{-1}\theta + \sec\theta\tan\theta),$$

$$\Phi_0 = -\frac{2}{\pi}S\,\mathrm{gd}^{-1}\theta, \tag{7.16}$$

where $\xi = \varepsilon S^3 = k^2\nu h v_{\mathrm{w}}^{-3}$ controls the exponential rate of decay as $y \to 1$. The superscript in Y_n^0 refers to the zero-order WKB expansion.

(c) The multiple-scale approach

Following the approach described by Majdalani (1998), we introduce two independent virtual coordinates, $y_0 = y$ and $y_1 = \varepsilon s(y)$, where 's' is an undetermined scale function that we propose to find. Note that the proposed transformation represents a slight departure from conventional linear transformations bearing the form $y_1 = \delta(\varepsilon)y$. The current stipulation of y_1 offers the necessary freedom that leads to a uniformly valid solution. Subsequently, functions and derivatives are expanded via

$$Y_n(y_0, y_1) = Y_0(y_0, y_1) + \varepsilon Y_1(y_0, y_1) + \mathcal{O}(\varepsilon^2), \quad \frac{\mathrm{d}}{\mathrm{d}y} = \frac{\partial}{\partial y_0} + \varepsilon\frac{\mathrm{d}s}{\mathrm{d}y_0}\frac{\partial}{\partial y_1},$$

$$\frac{\mathrm{d}^2}{\mathrm{d}y^2} = \frac{\partial^2}{\partial y_0^2} + \mathcal{O}(\varepsilon). \tag{7.17}$$

After substitution into (7.9), terms of the same order can be segregated to arrive at the following set of coupled partial differential equations:

$$\frac{\partial Y_0}{\partial y_0} + [\tfrac{1}{2}\pi(1+\lambda_n)\tan(\tfrac{1}{2}\pi y_0) - \mathrm{i}S\sec(\tfrac{1}{2}\pi y_0)]Y_0 = 0, \tag{7.18}$$

$$\frac{\partial Y_0}{\partial y_0} + [\tfrac{1}{2}\pi(1+\lambda_n)\tan(\tfrac{1}{2}\pi y_0) - \mathrm{i}S\sec(\tfrac{1}{2}\pi y_0)]Y_1 = -\frac{\mathrm{d}s}{\mathrm{d}y_0}\frac{\partial Y_0}{\partial y_1} + S\sec(\tfrac{1}{2}\pi y_0)\frac{\partial^2 Y_0}{\partial y_0^2}. \tag{7.19}$$

In much the same way, boundary conditions given by (7.10) can be converted into

$$Y_0(0) = 1, \quad \frac{\partial Y_0}{\partial y_0}(1) = 0. \tag{7.20}$$

Next, (5.2) can be integrated to produce

$$Y_0 = C_1(y_1)\exp\left\{(1+\lambda_n)\ln\cos(\tfrac{1}{2}\pi y_0) + \frac{2\mathrm{i}}{\pi}S\ln\tan[\tfrac{1}{4}\pi(1+y_0)]\right\} \equiv C_1(y_1)\chi(y_0), \tag{7.21}$$

where C_1 is an integration function that must be determined in a manner to ensure a converging series expansion in Y_n. Differentiating (7.21) and substituting the results

back into (7.19) gives

$$
\frac{\partial Y_1}{\partial y_0} + [\tfrac{1}{2}\pi(1+\lambda_n)\tan\theta_0 - iS\sec\theta_0]Y_1
$$

$$
= \left\{ -\frac{\mathrm{d}s}{\mathrm{d}y_0}\frac{\mathrm{d}C_1(y_1)}{\mathrm{d}y_1} + C_1(y_1)\sec\theta_0[-S^3\sec^2\theta_0 + \tfrac{1}{4}\pi^2(1+\lambda_n)(\lambda_n\tan^2\theta_0 - 1)S \right.
$$

$$
\left. - i\pi S^2(\tfrac{1}{2}+\lambda_n)\sec\theta_0\tan\theta_0] \right\}\chi(y_0), \quad (7.22)
$$

where $\theta_0 \equiv \tfrac{1}{2}\pi y_0$. Removing secular-producing terms requires that the right-hand side of (7.22) be zero. The resulting equation in C_1 can be easily integrated. In addition, satisfaction of (7.20) gives

$$
C_1(y) = \exp\{-\xi[\eta(y)\sec^3\theta - \eta(0)] + \xi\sigma^2\tfrac{1}{4}\pi^2(1+\lambda_n)
$$

$$
\times [\sec\theta\eta(y)(\lambda_n\tan^2\theta - 1) + \eta(0)] - i\pi\xi\sigma(\tfrac{1}{2}+\lambda_n)\eta(y)\sec^2\theta\tan\theta\}, \quad (7.23)
$$

where the viscous parameter $\xi = \varepsilon S^3$ makes its appearance here along with the effective scale functional $\eta(y)$. The latter is defined by

$$
\eta(y) \equiv s(y)/s'(y). \quad (7.24)
$$

The leading-order term can now be constructed from (7.23) and (7.21). In like fashion, further terms in the series of $\mathcal{O}(\varepsilon^2)$ can be obtained, but they become increasingly complicated. Since the overall solution is sought at $\mathcal{O}(M)$, and $M > \varepsilon$, there is no justification for retaining other than Y_0. Thus the expansion in (7.17) reduces to

$$
Y_n(y) = (\cos\theta)^{1+\lambda_n}\exp\left\{-\xi[\eta\sec^3\theta - \eta(0)]\right.
$$

$$
+ \frac{\pi^2}{4S^2}\xi(1+\lambda_n)[\eta\sec\theta(\lambda_n\tan^2\theta - 1) + \eta(0)]
$$

$$
\left. + \frac{2i}{\pi}S\ln\tan[\tfrac{1}{4}\pi(1+y)] - i\pi\frac{\xi}{S}(\tfrac{1}{2}+\lambda_n)\eta\sec^2\theta\tan\theta\right\} + \mathcal{O}(\varepsilon). \quad (7.25)
$$

The undetermined scale function remains, at present, unspecified. However, one can verify that, near the wall, an asymptotic solution exists for $s(y) = y$, as shown in detail by Majdalani (1998). Mathematically, this translates into

$$
\lim_{y\to 0}\eta(y) = y \Rightarrow \eta(0) = 0, \quad (7.26)
$$

which can be used to simplify (7.25) before substitution into (7.8). At the outset, one gets

$$
\tilde{u}(x,y,t) = -i\cos\theta\sum_{n=0}^{\infty}\frac{(-1)^n(k_m x\cos\theta)^{2n+1}}{(2n+1)!}
$$

$$
\times \exp\left\{-\xi\eta\sec^3\theta[1 + \tfrac{1}{4}\pi^2\sigma^2(2n+2)(\cos 2\theta + 2n\sin^2\theta)]\right.
$$

$$
\left. + \frac{2}{\pi}iS\ln\tan(\tfrac{1}{2}\theta + \tfrac{1}{4}\pi) - i\pi\xi\sigma(2n+\tfrac{3}{2})\eta\sec^2\theta\tan\theta - ik_m t\right\} + \mathcal{O}(\varepsilon),
$$

$$
(7.27)
$$

which is a rapidly converging series that displays distinctly terms of $\mathcal{O}(\sigma^2)$. In fact, the error associated with $n \geqslant 1$ terms is much smaller than the $\mathcal{O}(\varepsilon)$ entailed in the $n = 0$ term.

(d) Closed-form solution

Careful examination of (7.27) indicates that a closed-form equivalent is possible when terms that do not affect the reported precision are neglected. This can be accomplished by ignoring the $\mathcal{O}(\sigma^2)$ quantities arising in the $n \geqslant 1$ terms. The equivalent expression becomes

$$\tilde{u}(x, y, t) = -\mathrm{i} \cos \theta \sin(k_m x \cos \theta) \exp \zeta \exp[-\mathrm{i}(k_m t + \Phi)] + \mathcal{O}(\varepsilon), \qquad (7.28)$$

where

$$\zeta = \zeta_0 + \zeta_1 = -\xi \eta \sec^3 \theta - \tfrac{1}{2}\pi^2 \xi \sigma^2 \eta \sec^3 \theta \cos 2\theta, \qquad (7.29)$$

$$\Phi = \Phi_0 + \Phi_1 = -\frac{2}{\pi} S \ln \tan(\tfrac{1}{2}\theta + \tfrac{1}{4}\pi) + \tfrac{3}{2}\pi \xi \sigma \eta \sec^2 \theta \tan \theta. \qquad (7.30)$$

Clearly, each spatial damping function ζ and spatial phase angle Φ comprises a leading-order term and a small correction of $\mathcal{O}(\sigma^2)$.

(e) Other vortical components

Having obtained an accurate expression for $\tilde{u}$, the transverse component $\tilde{v}$ can be derived from mass conservation. Setting an ansatz of the form

$$\tilde{v}(x, y, t) = G(y) \cos(k_m x \cos \theta) \exp \zeta \exp[-\mathrm{i}(k_m t + \Phi)], \qquad (7.31)$$

$G(y)$ is a subsidiary function that must be determined in a manner to satisfy $\partial \tilde{u}/\partial x + \partial \tilde{v}/\partial y = 0$. After some manipulations, continuity is satisfied in leading-order quantities when $G = M v_0^3$. Henceforth,

$$\tilde{v}(x, y, t) = M \cos^3 \theta \cos(k_m x \cos \theta) \exp \zeta \exp[-\mathrm{i}(k_m t + \Phi)], \qquad (7.32)$$

indicating that the initial claim of $\tilde{v}/\tilde{u} = \mathcal{O}(M)$ was legitimate. This conclusion can also be verified numerically. In a similar fashion, temporal vorticity can be derived:

$$\tilde{\omega}(x, y, t) = -S \sin(k_m x v_0) \exp[\zeta - \mathrm{i}(k_m t + \Phi)]. \qquad (7.33)$$

(f) Specifying the undetermined scale

(i) *Velocity consideration*

One may proceed by contending that the multiple-scale formula should match, to leading order, the uniformly valid WKB expansion. This can be achieved by suppressing terms of $\mathcal{O}(\sigma^2)$ in (7.25) and equating the resulting expression to (7.16). At the outset, one finds

$$-\xi \eta \sec^3 \theta = -\frac{1}{\pi}\xi(\mathrm{gd}^{-1}\theta + \sec\theta\tan\theta) \quad \text{or} \quad \eta = \frac{1}{\pi}(\cos\theta\,\mathrm{gd}^{-1}\theta + \tan\theta)\cos^2\theta. \tag{7.34}$$

From (7.24), the appropriate scale function can be solved for via $s' - \eta^{-1}s = 0$. Recalling that $s(0) = 0$, direct integration yields

$$s(y) = \exp \int_0^y \eta^{-1}(\tau)\, d\tau = \sec(\tfrac{1}{2}\pi y)\tan(\tfrac{1}{2}\pi y) + \ln\tan\tfrac{1}{4}\pi(1+y). \qquad (7.35)$$

With this choice of s, the multiple-scale solution given by (7.28) will coincide with the corresponding WKB formulation when $\zeta_1 = \Phi_1 = 0$. Retention of the first-order corrections ζ_1 and Φ_1 in (7.28) slightly increases the accuracy of the multiple-scale formulation beyond its WKB counterpart.

(ii) *Vorticity consideration*

The current expression for vorticity can be compared with its counterpart in § 5 f. Knowing that the exponential decay of time-dependent vorticity must be affected by the same physical mechanisms irrespective of the perturbation technique, the spatial damping function ζ must be the same as that obtained previously. This implies that, in (7.29), we must have

$$-\xi\eta\sec^3(\tfrac{1}{2}\pi y) = -\frac{1}{\pi}\xi[\ln\tan\tfrac{1}{4}\pi(1+y) + \sec(\tfrac{1}{2}\pi y)\tan(\tfrac{1}{2}\pi y)], \qquad (7.36)$$

which leads to the same expressions obtained from velocity consideration.

(iii) *Comparison with previous work*

Fortuitously, we are able to obtain, this time, an exact expression for the nonlinear transformation, $y_1 = \varepsilon s(y)$, that leads to a uniformly valid multiple-scale solution. The complexity of formula (7.35) precludes the possibility of guessing this coordinate transformation beforehand, as demanded by conventional multiple-scale procedures. It also justifies the need to employ the 'reverse engineering' process in determining the scales. The most striking result is, perhaps, the agreement with the ad hoc formulation obtained by Majdalani (1998). In the previous analysis, a composite scale $s(y) = y(1-y)^{-3y^{3/2}/2}$ was constructed in such a manner as to reproduce asymptotically the inner, outer and intermediate scales that appeared in the problem. As a result, usage of the composite scale reduced the number of spatial scales to two, which was necessary for the success of the multiple-scale expansion. At the outset, the effective scale functional η was derived and then substituted into the solution. In the current analysis, η is determined first, and it is only at the conclusion of the analysis that one may verify that the space-reductive coordinate does indeed reduce to the proper spatial scales in their regions of applicability. For instance, in the vicinity of the transpiring wall and core, one can recover the scales found by Majdalani (1998). Thus,

$$y_1 = \varepsilon[\sec(\tfrac{1}{2}\pi y)\tan(\tfrac{1}{2}\pi y) + \ln\tan\tfrac{1}{4}\pi(1+y)] \rightarrow \begin{cases} \varepsilon y, & y \rightarrow 0, \\ \varepsilon(1-y)^{-2}, & y \rightarrow 1. \end{cases} \qquad (7.37)$$

For the sake of illustration, η and s obtained herein are compared in figure 7 with their counterparts from Majdalani (1998). Clearly, predictions from the multiple-scale solution agree with those obtained previously using the composite-scale technique.
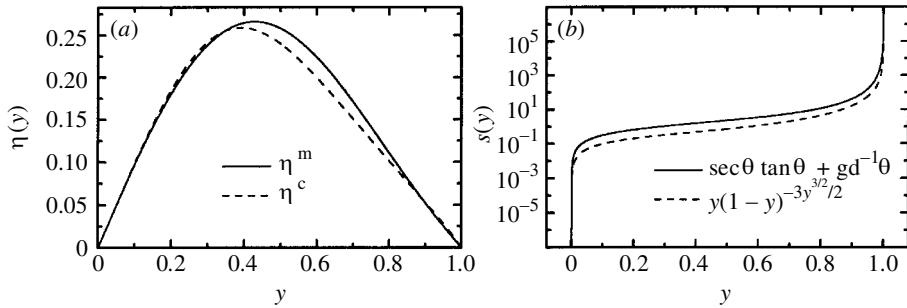
Figure 7. Comparing the effective scale functional η in (a) and corresponding scale function s in (b) to existing composite results given by Majdalani (1998). Superscripts refer to 'multiple' or 'composite' scale solutions.

8. Results and discussion

(a) *The oscillatory velocity profile*

Since $\tilde{v}/\tilde{u} = \mathcal{O}(M)$, $\tilde{u}$ dominates the rotational field, and the temporal velocity can be obtained by adding both irrotational and rotational contributions. The result, from (7.28), is

$$u_1(x, y, t) = \mathrm{i}\{\sin(k_m x)\exp(-\mathrm{i}k_m t) - \cos\theta\sin(k_m x\cos\theta)\exp[\zeta - \mathrm{i}(k_m t + \Phi)]\}. \tag{8.1}$$

As Euler's notation is no longer needed, it is more convenient to focus on the real part of (8.1):

$$u_1(x, y, t) = \overbrace{\sin(k_m x)\sin(k_m t)}^{\text{irrotational part}} - \overbrace{\underbrace{\cos\theta\sin(k_m x\cos\theta)\exp\zeta}_{\text{wave amplitude}}\ \underbrace{\sin(k_m t + \Phi)}_{\text{wave propagation}}}^{\text{rotational part}}. \tag{8.2}$$

The first term in (8.2) denotes the pressure-driven inviscid response and the second term represents the vorticity-driven viscous response. In concurrence with conventional theory, formula (8.2) assumes a traditional form encountered in studies of periodic flows of the Stokes type, reminiscent of equation (10.3) in Rott (1964). As such, it displays the vortical wave characteristics that permit explicit formulations for the vortical depth of penetration, velocity overshoot and surfaces of constant phase. Unlike theoretical studies that are concerned with infinitely long channels with oscillatory motions induced by pistons at infinity, a dependence on the axial coordinate x is caused here by the body's finite length. Further examination of (8.2) reveals that the vortical amplitude is affected by two separate terms: an exponentially damped function due to viscous dissipation; and a space-harmonic function due to the axial mean flow convection of temporal vorticity. While both terms decrease with increasing distance from the wall, the latter varies sinusoidally in the streamwise direction. Moreover, inspection of the spatial damping function ζ reveals that successive increases in viscosity reduce the rotational strength.
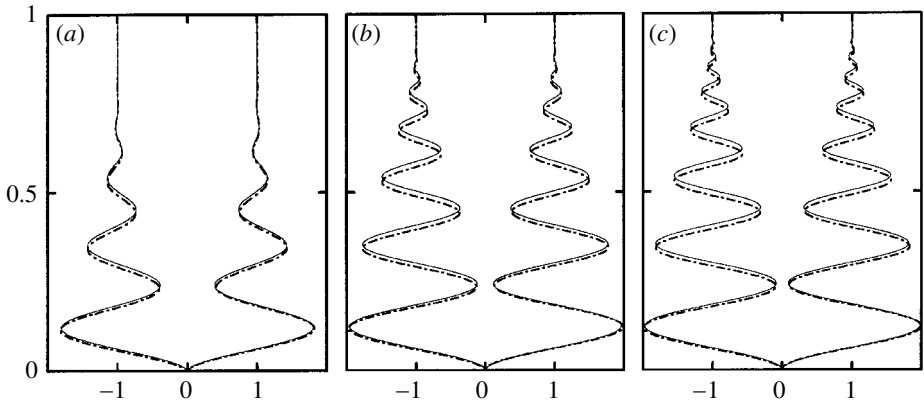
Figure 8. Comparing the asymptotic solution (full curves) to numerical computations of the non-linear Navier–Stokes equations (chain curves) at two successive times. Here $S = 25$, $x/l = 1/2$, and $m = 1$. Using a 40×300 mesh resolution, simulation results are shown after nine iteration cycles for (a) $K = 10^4$, (b) $K = 10^5$, and (c) $K = 10^6$.

(b) Comparison with computational data

In order to ensure the validity of our asymptotics, we insist on comparisons with computational predictions. These are obtained from a dual time-stepping code, developed totally independently by Roh *et al.* (1995). The code is devoted to analysing gas-phase processes based on the complete conservation equations of mass, momentum and energy. When executed, the algorithm uses pressure decomposition and precon-ditioning techniques to circumvent difficulties encountered in low-speed compressible flows. Subsequently, the set of governing equations with appropriate boundary con-ditions is solved numerically by means of a finite-volume approach. A fully coupled implicit formulation is further used to enhance numerical stability and efficiency. The scheme has the advantage of achieving a high degree of temporal accuracy with only a modest increase in computational cost. Moreover, since the governing equations are solved implicitly, the numerical method is stable. As a result, the selection of the integration time-step is dictated by the individual process, and not by stability constraints.

For the same physical parameters used in our asymptotic formulae, numerical sim-ulations are monitored until convergence is ensured. Results obtained for a number of test cases are found to be quite satisfactory. For illustration purposes, we show in figure 8 both asymptotics and numerics at three orders of the kinetic Reynolds num-ber. Cases corresponding to $K = 10^7$ and higher become nearly inviscid and bear a striking resemblance to figure 8c. In every case, the velocity profiles, characterized by oscillations that progressively decay from the wall, are depicted at two successive times separated by a $\frac{1}{2}\pi$ phase difference. The small disparity between theoretical and computational data can be attributed to small discretization errors and non-linearity effects that elude our analytic formulation. This agreement is consistent at higher modes where an increasing number of cycles is required. In the absence of an exact solution to the case at hand, this comparison to a full Navier–Stokes solution is pivotal.

Table 1. *Oscillatory velocity predictions for $S = 50$, $K = 10^6$, $k_m t = \frac{1}{2}\pi$, $x/l = \frac{1}{2}$ and $m = 1$*

y	numeric	(5.31) asymptotic	(8.2) asymptotic	(5.31) error (%)	(8.2) error (%)
0.00	0.000 00	0.000 00	0.000 00	0.000 00	0.000 00
0.05	1.795 17	1.795 19	1.795 16	0.001 05	0.000 51
0.10	0.704 21	0.704 18	0.704 30	0.005 08	0.012 27
0.15	0.733 20	0.733 23	0.732 98	0.003 76	0.029 96
0.20	1.679 81	1.679 81	1.680 09	0.000 13	0.016 83
0.25	0.144 82	0.144 80	0.144 65	0.016 50	0.116 03
0.30	1.835 52	1.835 57	1.835 41	0.002 63	0.006 10
0.35	0.272 91	0.272 82	0.273 35	0.029 91	0.162 26
0.40	1.626 42	1.626 55	1.625 74	0.008 07	0.042 05
0.45	0.420 48	0.420 31	0.421 18	0.042 76	0.165 82
0.50	1.563 96	1.564 11	1.563 64	0.009 39	0.020 37
0.55	0.530 14	0.530 30	0.529 58	0.029 91	0.105 54
0.60	1.140 62	1.139 81	1.142 04	0.070 86	0.124 12
0.65	1.271 83	1.272 44	1.271 21	0.047 72	0.048 85
0.70	0.964 05	0.965 48	0.963 23	0.147 45	0.085 47
0.75	0.930 11	0.931 69	0.929 84	0.170 65	0.028 19
0.80	1.042 57	1.044 24	1.042 80	0.160 40	0.022 56
0.85	0.989 24	0.987 34	0.988 39	0.192 49	0.086 01
0.90	0.996 54	0.995 49	0.995 82	0.105 54	0.072 38
0.95	0.999 95	1.000 01	1.000 00	0.005 46	0.005 12
1.00	1.000 00	1.000 00	1.000 00	0.000 00	0.000 00

(c) Comparison with both theoretical and numerical data

In table 1, we now compare numerical simulations of the linearized Navier–Stokes equations (described in § 5 a) to the asymptotic results, given by (5.31) and (8.2). We select a test case with flow parameters that fall in the middle of the physical range under investigation. The last two columns give the percentage deviation of the preceding entries relative to numerical approximations. It is very satisfying to note the agreement, in many cases, to three or more decimal places, between theoretical and numerical predictions.

(d) Wave characteristics

For the purpose of confirming the agreement between (5.31) and (8.2), the maximum velocity overshoot factor that occurs near the wall is quantified in figure 9. Practically, the calculated overshoot is the same, in both magnitude and location, irrespective of the formulation used. As discussed earlier, this phenomenon is a key feature of periodic flows that appears to be far more significant in the presence of wall injection.

From (8.2), the normal speed of propagation of rotational waves, dy^*/dt^*, can be determined explicitly due to the compact formulation. The wave speed is thus found to match the steady flow velocity $(v_w v_0)$. Forthwith, the normalized spatial wavelength can be determined to be $(2\pi v_0/S)$. This implies progressively diminishing
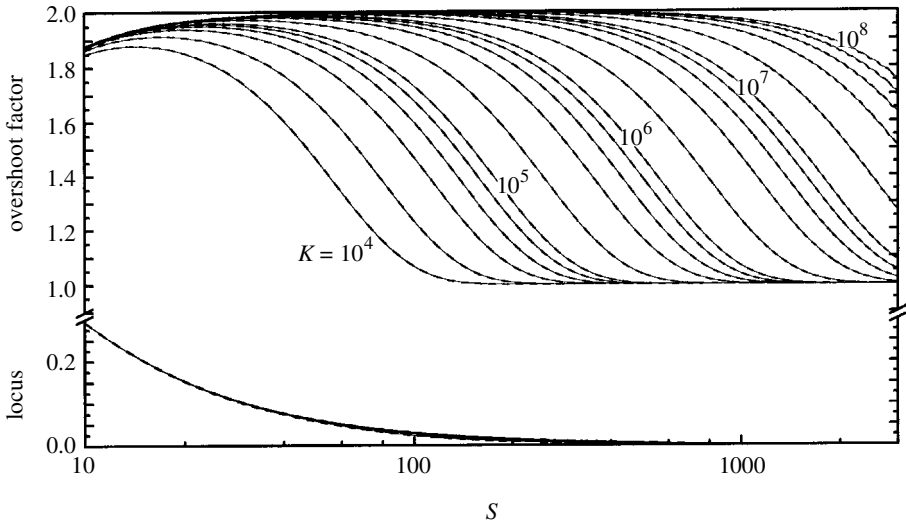
Figure 9. For the first oscillation mode, we compare the Richardson velocity overshoot in both magnitude and location over a wide spectrum of physical parameters half way across the channel. To the accuracy of the graph, predictions from (5.31) and (8.2) are indistinguishable.

vortical wavelengths near the core, where v_0 is small, and at high Strouhal numbers. This also explains the need to refine the computational mesh near the core to capture the rotational effects occurring at increasingly smaller length-scales.

Unlike (5.31), (8.2) permits definition of the surfaces of constant phase in closed form. From the wave propagation term, we consider $\cos k_m(t + \Phi/k_m) = \text{const.}$, and derive, by way of the Gudermannian function, the equation for the characteristic surfaces at various c values:

$$y = \frac{4}{\pi} \arctan[\tfrac{1}{2}\pi M(t - c)] - 1.$$

(e) Penetration depth

The penetration depth Δ can be defined to be the normalized distance from the wall to the point where 99% of the rotational wave amplitude in (8.2) would have vanished. As the viscous layer delineates two essentially inviscid zones, a rotational zone near the wall and an irrotational zone near the core, Δ may serve to also locate the blown-off layer. If one defines the point $y = \Delta$ above the wall where the rotational amplitude reduces to $\alpha = 1\%$ of its irrotational counterpart, then Δ is soluble from

$$\cos(\tfrac{1}{2}\pi\Delta)\sin[k_m x\cos(\tfrac{1}{2}\pi\Delta)]\exp[-\eta(\Delta)\xi\sec^3(\tfrac{1}{2}\pi\Delta)] - \alpha|\sin(k_m x)| = 0. \qquad (8.3)$$

Despite its transcendental form, (8.3) indicates that the exponential decay is a strong function of a dimensionless penetration number, $\Lambda = \xi^{-1}$. This observation suggests generating curves of Δ versus Λ for large variations in K and S. In fact, figure 10 shows how entire families of asymptotic curves over wide ranges of K and S collapse into single curves per axial position. Here too, asymptotics and numerics concur. This interesting result reveals that Δ does not depend on K and S separately, but rather on $\Lambda = KS^{-3}$. This parameter resembles, in importance, the Stokes or Womersley
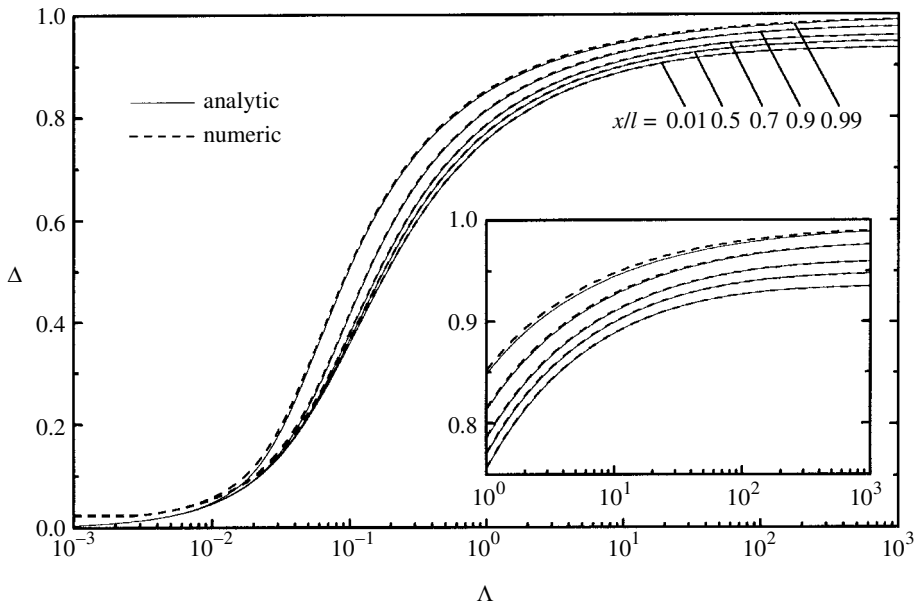
Figure 10. Penetration depth for a wide range of parameters and axial locations including both numerical ($K = 10^6$) and asymptotic predictions ($10^4 < K < 10^8$). Part of the graph is enlarged in the inset.

numbers in periodic flows over hard walls. Physically, it represents the relative intensity of time-dependent inertia to viscous diffusion in the cross-streamwise direction. The pertinent ratio scales with

$$\frac{\text{temporal inertia}}{\text{viscous force}} \approx \frac{\rho \dfrac{\partial v}{\partial t}}{\mu \dfrac{\partial^2 u}{\partial y^2}} \approx \frac{\rho \dfrac{v_{\text{w}}}{(1/k)}}{\mu \dfrac{kh}{(v_{\text{w}}/k)^2}} = \frac{v_{\text{w}}^3}{h\nu k^2} \equiv \Lambda. \tag{8.4}$$

Figure 10, along with formula (8.3), brings into focus the character of the rotational penetration depth over permeable walls. For instance, it is clear that Δ depends on Λ, m and, to a lesser degree, on the axial station, especially within the aft portion of the channel. For small Λ, the penetration depth Δ varies linearly with the penetration number Λ, irrespective of x. Apparently, the larger the penetration number, the larger the penetration depth will be. This dimensionless group reveals that increasing injection, or decreasing viscosity, frequency or channel height broadens the depth of penetration. The time-dependent solution thus represents a strongly damped wave whose penetration depth into the fluid is inversely proportional to ν. This is in sharp contrast to the depth of penetration of periodic flows over impermeable walls, where the dependence on the kinematic viscosity is the same as in boundary-layer theory, namely, proportional to $\sqrt{\nu}$.

As borne out in the graph, for sufficiently large Λ, Δ approaches a maximum fixed value per axial station. In order to locate this maximum possible depth, $\Delta_{\infty}(m,x) = \Delta(\Lambda \to \infty, m, x)$, we note that, for the ideal case of zero viscosity, rotational waves face minimum resistance and, thereby, travel the furthest distance from the wall. This asymptotic limit can thus be evaluated from the inviscid formulation of the

penetration depth, which only depends on the axial station and pressure oscillation mode. From (8.3), one obtains

$$\cos(\tfrac{1}{2}\pi\Delta_\infty)\sin[k_m x \cos(\tfrac{1}{2}\pi\Delta_\infty)] - \alpha|\sin(k_m x)| = 0. \tag{8.5}$$

Solving for the inviscid penetration depth from (8.5), we get

$$\Delta_\infty(m,x) = 1 - \frac{2}{\pi}\sqrt{\alpha|\sin(k_m x)|k_m^{-1}x^{-1}} + \mathcal{O}(1-\Delta_\infty)^3, \tag{8.6}$$

which exhibits a maximum absolute error of 2.62×10^{-4} when $\Delta_\infty(1,0) = 0.9364$. In practice, this expression can be quite useful, being correct to $\mathcal{O}(10^{-4})$.

(f) Asymptotic error behaviour

In arriving at the final asymptotic formulation set out in (5.31), a number of successive approximations were made that introduced uncertainty in the total cumulative error. In order to remove this uncertainty, one may refer to a technique described by Bosley (1996). In fact, Bosley's technique provides a rigorous verification for the order of the error incurred in the derivation. To that end, the maximum error E_m can be defined to be the maximum absolute difference between u_1 given asymptotically and u_1^n computed numerically. Then for every m, S and K, one can calculate, over a complete oscillation cycle,

$$E_m(m,S,K) = \max_{\substack{0\leqslant x\leqslant 1 \\ 0\leqslant y\leqslant 1}} |u_1^n(x,y,t,m,S,K) - u_1(x,y,t,m,S,K)|. \tag{8.7}$$

Suspecting that the error could be of $\mathcal{O}(K^{-\alpha})$, one can assume an error variation of the form

$$E_m(m,S,K) = \beta(m,S)(1/K)^\alpha \tag{8.8}$$

and determine the slope α from the log–log plot of E_m versus $1/K$.

Results are shown in figure 11 at several values of the Strouhal number. The errors associated with (5.31) and (8.2) are compared in figure 11*b* and show a slight improvement in the error associated with the multiple-scale formulation. As one can infer from the graph, the slope of the maximum error approaches one asymptotically irrespective of S. This result has been confirmed using the method of least squares in decreasing ranges of ε, but is omitted here for brevity. The consistent asymptotic behaviour is gratifying and, according to Bosley (1996), indicates that both asymptotic formulations are legitimate uniformly valid expansions. Overall, both remain at $\mathcal{O}(\varepsilon)$. It is reassuring to note that $\varepsilon < M$ is the smallest naturally occurring perturbation parameter encountered heretofore. Overall, it must not be forgotten that the error associated with the governing differential equation is only correct to $\mathcal{O}(M)$, and so will the final formulations.

9. Concluding remarks

In the current paper we have considered the effects of unsteadiness caused by small-amplitude pressure oscillations about the classic Taylor flow in a porous channel. We have specifically excluded questions regarding hydrodynamic stability or turbulence in order to manage a basic laminar solution for large wall injection. We
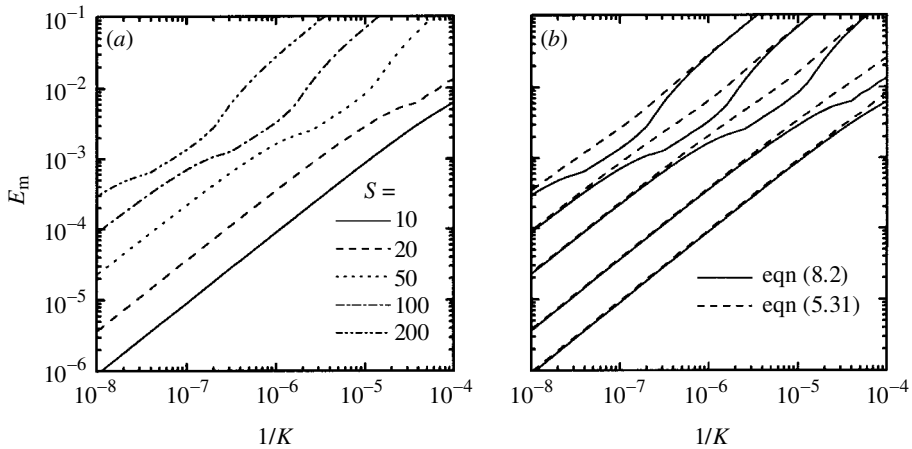
Figure 11. Asymptotic behaviour of the maximum absolute error between numerical and asymptotic predictions for the fundamental oscillation mode. The error curves shown correspond to (*a*) the multiple-scale solution, and (*b*) both asymptotic solutions.

have exploited a popular method that breaks down the analysis into a steady fundamentally nonlinear solution and a superimposed linearized time-dependent part. Expressions were derived from both the vorticity and momentum transport equations. The accurate analytic formulae obtained were instrumental in revealing rich vortical structures that are byproducts of mean and time-dependent flow interactions. They also revealed dimensionless parameters that control the flow character. By way of validation, comparisons to numerical solutions of the Navier–Stokes equations were reassuring. Comparisons with the exact solution arising in the analogous setting with impermeable walls were also favourable. A formal assessment of the maximum error entailed at the conclusion of the asymptotic analysis revealed an unexpected bonus. The error was found to be very small as it varied with the reciprocal of the kinetic Reynolds number. The interesting mathematical aspect of this investigation, that could possibly be extended to other practical problems, is the way in which the inclusion of an undetermined scale can lead to the nonlinear scaling transformation.

References

Abramowitz, M. & Stegun, I. A. 1964 *Handbook of mathematical functions*, p. 77. National Bureau of Standards. New York: Dover.

Avalon, G., Casalis, G. & Griffond, J. 1998 Flow instabilities and acoustic resonance of channels with wall injection. AIAA paper 98-3218.

Barron, J., Majdalani, J. & Van Moorhem, W. K. 1998 A novel investigation of the oscillatory field over a transpiring surface. AIAA paper 98-2694.

Berman, A. S. 1953 Laminar flow in channels with porous walls. *J. Appl. Phys.* **24**, 1232–1235.

Bosley, D. L. 1996 A technique for the numerical verification of asymptotic expansions. *SIAM Rev.* **38**, 128–135.

Brady, J. F. 1984 Flow development in a porous channel or tube. *Phys. Fluids* **27**, 1061–1067.

Carrier, B. T. & Carlson, F. D. 1946 On the propagation of small disturbances in a moving compressible fluid. *Q. Appl. Math.* **4**, 1–12.

Casalis, G., Avalon, G. & Pineau, J.-P. 1998 Spatial instability of planar channel flow with fluid injection through porous walls. *Phys. Fluids* **10**, 2558–2568.

Chu, B.-T. & Kovásznay, L. S. G. 1957 Non-linear interactions in a viscous heat-conducting compressible gas. *J. Fluid Mech.* **3**, 494–514.

Cox, S. M. 1991 Two-dimensional flow of a viscous fluid in a channel with porous walls. *J. Fluid Mech.* **227**, 1–33.

Cox, S. M. & King, A. C. 1997 On the asymptotic solution of a high-order nonlinear ordinary differential equation. *Proc. R. Soc. Lond.* A **453**, 711–728.

Durlofsky, L. & Brady, J. F. 1984 The spatial stability of a class of similarity solutions. *Phys. Fluids* **27**, 1068–1076.

Hastings, S. P., Lu, C. & MacGillivray, A. D. 1992 A boundary value problem with multiple solutions from the theory of laminar flow. *SIAM Jl Math. Analysis* **23**, 201–208.

Hocking, L. M. 1975 Non-linear instability of the asymptotic suction velocity profile. *Q. Jl Mech. Appl. Math.* **28**, 341–353.

Lighthill, M. J. 1954 The response of laminar skin friction and heat transfer to fluctuations in the stream velocity. *Proc. R. Soc. Lond.* A **224**, 1–23.

Lu, C., MacGillivray, A. D. & Hastings, S. P. 1992 Asymptotic behaviour of solutions of a similarity equation for laminar flows in channels with porous walls. *IMA Jl Appl. Math.* **49**, 139–162.

Ma, Y., Van Moorhem, W. K. & Shorthill, R. W. 1991 Experimental investigation of velocity coupling in combustion instability. *J. Propul. Power* **7**, 692–699.

MacGillivray, A. D. & Lu, C. 1994 Asymptotic solution of a laminar flow in a porous channel with large suction: a nonlinear turning point problem. *Meth. Appl. Analysis* **1**, 229–248.

Majdalani, J. 1998 A hybrid multiple scale procedure for boundary layers involving several dissimilar scales. *J. Appl. Math. Phys.* **49**, 849–868.

Morduchow, M. 1957 On laminar flow through a channel or tube with injection: application of method of averages. *Q. Jl Appl. Math.* **14**, 361–368.

Proudman, I. 1960 An example of steady laminar flow at large Reynolds number. *J. Fluid Mech.* **9**, 593–612.

Raithby, G. D. & Knudsen, D. C. 1974 Hydrodynamic development in a duct with suction and blowing. *Trans. Am. Soc. Mech. Engnrs: J. Appl. Mech.* E **41**, 896–902.

Richardson, E. G. 1928 The amplitude of sound waves in resonators. *Proc. Phys. Soc.* **40**, 206–220.

Richardson, E. G. & Tyler, E. 1929 The transverse velocity gradient near the mouths of pipes in which an alternating or continuous flow of air is established. *Proc. R. Soc. Lond.* A **42**, 1–15.

Robinson, W. A. 1976 The existence of multiple solutions for the laminar flow in a uniformly porous channel with suction at both walls. *J. Engng Math.* **10**, 23–40.

Roh, T. S., Tseng, I. S. & Yang, V. 1995 Effects of acoustic oscillations on flame dynamics of homogeneous propellants in rocket motors. *J. Propul. Power* **11**, 640–650.

Rott, N. 1964 Theory of time-dependent laminar flows. In *High speed aerodynamics and jet propulsion—theory of laminar flows* (ed. F. K. Moore), vol. IV, pp. 395–438. Princeton University Press.

Sellars, J. R. 1955 Laminar flow in channels with porous walls at high suction Reynolds numbers. *J. Appl. Phys.* **26**, 489–490.

Shih, K.-G. 1987 On the existence of solutions of an equation arising in the theory of laminar flow in a uniformly porous channel with injection. *SIAM Jl Appl. Math.* **47**, 526–533.

Skalak, F. M. & Wang, C.-Y. 1978 On the non-unique solutions of laminar flow through a porous tube or channel. *SIAM Jl Appl. Math.* **34**, 535–544.

Sviridenkov, A. A. & Yagodkin, V. I. 1976 Flow in the initial sections of channels with permeable walls. *Fluid Dyn. (Izv. AN SSSR. MZhG)* **11**, 689–693.

Taylor, C. L., Banks, W. H. H., Zaturska, M. B. & Drazin, P. G. 1991 Three-dimensional flow in a porous channel. *Q. Jl Mech. Appl. Math.* **44**, 105–133.

Taylor, G. I. 1956 Fluid flow in regions bounded by porous surfaces. *Proc. R. Soc. Lond.* A **234**, 456–475.

Terrill, R. M. 1964 Laminar flow in a uniformly porous channel. *Aero. Quart.* **15**, 299–310.

Terrill, R. M. 1965 Laminar flow in a uniformly porous channel with large injection. *Aero. Quart.* **16**, 323–332.

Varapaev, V. N. & Yagodkin, V. I. 1969 Flow stability in a channel with porous walls. *Fluid Dyn. (Izv. AN SSSR. MZhG)* **4**, 91–95.

Watson, P., Banks, W. H. H., Zaturska, M. B. & Drazin, P. G. 1991 Laminar channel flow driven by accelerating walls. *Eur. Jl Appl. Math.* **2**, 359–385.

White Jr, F. M., Barfield, B. F. & Goglia, M. J. 1958 Laminar flow in a uniformly porous channel. *Trans. Am. Soc. Mech. Engnrs: J. Appl. Mech.* E **25**, 613–617.

Yuan, S. W. 1956 Further investigation of laminar flow in channels with porous walls. *J. Appl. Phys.* **27**, 267–269.

Zaturska, M. B., Drazin, P. G. & Banks, W. H. H. 1988 On the flow of a viscous fluid driven along a channel by suction at porous walls. *Fluid Dyn. Res.* **4**, 151–178.